University of Kentucky
UKnowledge

Theses and Dissertations--Mechanical Engineering

Mechanical Engineering

2023

Stratospheric Glider Measurements of Atmospheric Parameters

Anisa Haghighi
University of Kentucky, anisa90@gmail.com
Digital Object Identifier: https://doi.org/10.13023/etd.2023/479

Right click to open a feedback form in a new tab to let us know how this document benefits you.

Recommended Citation

Haghighi, Anisa, "Stratospheric Glider Measurements of Atmospheric Parameters" (2023). *Theses and Dissertations--Mechanical Engineering*. 216.
https://uknowledge.uky.edu/me_etds/216

This Master's Thesis is brought to you for free and open access by the Mechanical Engineering at UKnowledge. It has been accepted for inclusion in Theses and Dissertations--Mechanical Engineering by an authorized administrator of UKnowledge. For more information, please contact UKnowledge@lsv.uky.edu.

STUDENT AGREEMENT:

I represent that my thesis or dissertation and abstract are my original work. Proper attribution has been given to all outside sources. I understand that I am solely responsible for obtaining any needed copyright permissions. I have obtained needed written permission statement(s) from the owner(s) of each third-party copyrighted matter to be included in my work, allowing electronic distribution (if such use is not permitted by the fair use doctrine) which will be submitted to UKnowledge as Additional File.

I hereby grant to The University of Kentucky and its agents the irrevocable, non-exclusive, and royalty-free license to archive and make accessible my work in whole or in part in all forms of media, now or hereafter known. I agree that the document mentioned above may be made available immediately for worldwide access unless an embargo applies.

I retain all other ownership rights to the copyright of my work. I also retain the right to use in future works (such as articles or books) all or part of my work. I understand that I am free to register the copyright to my work.

REVIEW, APPROVAL AND ACCEPTANCE

The document mentioned above has been reviewed and accepted by the student's advisor, on behalf of the advisory committee, and by the Director of Graduate Studies (DGS), on behalf of the program; we verify that this is the final, approved version of the student's thesis including all changes required by the advisory committee. The undersigned agree to abide by the statements above.

Anisa Haghighi, Student

Dr. Sean Bailey, Major Professor

Dr. Jonathan Wenk, Director of Graduate Studies

Stratospheric Glider Measurements of Atmospheric Parameters

THESIS

A thesis submitted in partial
fulfillment of the requirements for
the degree of Master of Science in
the College of Engineering at the
University of Kentucky

By
Anisa Haghighi Najafabadi
Lexington, Kentucky

Director: Dr. Sean Bailey, Professor of Mechanical and Aerospace Engineering
Lexington, Kentucky
2023

Copyright© Anisa Haghighi Najafabadi 2023

ABSTRACT OF DISSERTATION

Stratospheric Glider Measurements of Atmospheric Parameters

In June 2021 a series of high altitude flights were conducted in Spaceport America, NM, using a balloon launched Uncrewed Aircraft System (UAS) to assess its capability to conduct measurements of various atmospheric properties and study turbulence in the troposphere and lower stratosphere. This UAS descends using an automated flight trajectory. The instruments aboard included a NASA-developed infrasonic microphone to evaluate its remote turbulence detection capabilities and a five-hole probe capable of measuring the in situ wind vector. Also on board were temperature, humidity and wind profile sensors. This document focuses on the atmospheric properties measured at high altitudes, the use of these properties to calculate different turbulence statistics, stability parameters and their connection to the turbulence using the five-hole probe measurements. By being able to transect the air, the glider allows for turbulence wavelengths to be sampled at a particular altitude, improving statistical convergence and spatial resolution of derived statistics from its in-situ sensors. The results show that the temperature and relative humidity agree well with conventional radiosonde measurements made by nearby National Weather Service stations. In addition, the results show that in-situ measurements using this type of UAS can be an effective tool for measuring atmospheric wind and turbulence.

KEYWORDS: stratosphere, turbulence, uncrewed aerial systems (UAS), remote sensing

Anisa Haghighi Najafabadi

December 8, 2023

Stratospheric Glider Measurements of Atmospheric Parameters

By

Anisa Haghighi Najafabadi

Dr. Sean Bailey

Director of Dissertation

Dr. Jonathan Wenk

Director of Graduate Studies

December 8, 2023

Date

ACKNOWLEDGMENTS

I would like to express my deepest appreciation to my advisor, Dr. Sean Bailey, for giving me this opportunity and who has been a great mentor and has guided me through my research. He has provided me with invaluable patience and consistent support and guidance. I would also like to thank my family who have been a great support in the past few years and continue to be so. Furthermore, I would like to thank Ryan Nolin at the UAV lab and Gary Pundsack and Nick Craine at Stratodynamics for making the test flights happen. Their work has enabled me to conduct this research. I would also like to thank the late Dr. Qamar Shams who worked at NASA Langley Research Center and graciously assisted with the implementation and the loan of the infrasonic microphone from NASA.

Finally, I would like to thank NASA under the Flight Opportunities Program who supported this research through award number 80NSSC20K0102.

TABLE OF CONTENTS

Acknowledgments iii

List of Tables vi

List of Figures vii

Chapter 1 Introduction 1
1.1 Turbulence 1
1.2 Atmospheric Turbulence and its Detection 2
1.3 Atmospheric Turbulence Measurement 3
1.4 Research Objective 5

Chapter 2 Background 7
2.1 Navier-Stokes Equation 7
2.2 Turbulent Kinetic Energy 8
2.3 Turbulent Kinetic Energy Dissipation Rate 9
2.4 Energy Spectrum of Turbulence 9
2.4.1 Atmospheric Gravity Waves 11
2.4.2 Brunt-Väisälä Frequency and Richardson Number 12
2.5 In-situ Measurements of Stratospheric Turbulence 13

Chapter 3 Experiment 16
3.1 Overview 16
3.1.1 Aircraft 17
3.1.2 Payload 18
3.1.3 Flight Profiles: 23

Chapter 4 In-situ Measurement of Atmospheric Turbulence using the Five-Hole Probe 25
4.1 Mean Quantities 25
4.1.1 Stability Conditions 30
4.2 Local Turbulence Measurement 33

Chapter 5 Conclusions and Future Work 41

Appendix: Upper Air Maps 43

Bibliography 44

Vita 52

LIST OF TABLES

4.1 EDR ranges identified to correspond to different turbulence intensities. . 39
4.2 Turbulence location, intensity and production mechanism summary for Flight 1. 40
4.3 Turbulence location, intensity and production mechanism summary for Flight 2. 40
4.4 Turbulence location, intensity and production mechanism summary for Flight 3. 40

LIST OF FIGURES

2.1 The model spectra in one-dimensional form showing the different subranges at an arbitrarily high Reynolds number. 12

3.1 The topography of the flight area with Spaceport America with the area encompassed by the flight indicated by a white circle. 16

3.2 Images of HiDRON H2 showing: (a) close up of aircraft nose showing five-hole probe and temperature and humidity sensor location; (b) aircraft during launch; and (c) aircraft during landing. 17

3.3 Horizontal ground speed in inertial Earth-fixed coordinates, $|\vec{V}_G|$, magnitude of the descent speed in inertial Earth-fixed coordinates and relative air velocity magnitude in aircraft-fixed coordinates, $|\vec{V}_R|$, for (a) Flight 1, (b) Flight 2 and (c) Flight 3. 19

3.4 (a) Five-hole probe, (b) infrasonic microphone, and (c) nose payload bay open between flights, with embedded computer shown removed for data retrieval. Infrasonic microphone is below embedded computer but was installed in aircraft nose facing forward during flight. 19

3.5 HiDRON H2 flight trajectory for (a) Flight 1, (b) Flight 2 and (c) Flight 3. Trajectory is colored by time, with lighter color indicating earliest phase of balloon ascent. z indicates height above ground level (a.g.l.) 24

4.1 Temperature profiles measured during (a) Flight 1; (b) Flight 2; and (c) Flight 3. Corresponding relative humidity profiles shown for (d) Flight 1; (e) Flight 2; and (f) Flight 3. 27

4.2 Horizontal wind magnitude a measured during (a) Flight 1; (b) Flight 2; and (c) Flight 3. Corresponding wind direction shown for (d) Flight 1; (e) Flight 2; and (f) Flight 3. 28

4.3 Brunt–Väisälä frequency, N_t and N_z, profiles for (a) Flight 1; (b) Flight 2; and (c) Flight 3 and shear frequency, S_t and S_z^2, profiles for (d) Flight 1; (e) Flight 2; and (f) Flight 3. 31

4.4 Gradient Richardson number, Ri_t and Ri_z, profiles for (a) Flight 1; (b) Flight 2; and (c) Flight 3. The vertical lines indicate $Ri = 0.25$ and $Ri = 1$, denoting the possible range of critical Richardson numbers. . . . 32

4.5 Profiles of k for (a) Flight 1, (b) Flight 2, and (c) Flight 3. Corresponding profiles of EDR are shown for (d) Flight 1, (e) Flight 2, and (f) Flight 3. Solid red symbols indicate measurements where $-1.8 < n < -1.5$. Dashed lines indicate qualitative turbulence intensity levels from [36] referred to as: steady for $EDR < 0.1$; weak for EDR between 0.1 and 0.3; moderate for EDR between 0.3 and 0.5; strong for EDR between 0.5 and 0.8; and very strong for $EDR > 0.8$. 35

4.6 Example longitudinal velocity spectra from Flight 1 at (a) $z = 1$ km, (b) $z = 10$ km, and (c) $z = 18$ km. Red lines indicate fit, blue lines indicate $f^{-5/3}$ slope. Only content for wavenumbers corresponding to $f < 20$ Hz are shown. 36

Chapter 1 Introduction

Turbulence is the chaotic behavior of a fluid that, although deterministic in nature, is highly dependent on the fluid properties and the boundary conditions associated with its production [51]. It is therefore challenging to model and predict with reliable fidelity.

In the atmosphere, the non-stationary nature of the atmosphere itself [64] and the numerous boundary conditions that influence its behavior make the study of turbulence within it even more challenging. However atmospheric turbulence is of particular interest as it not only is significant for meteorology, but from an engineering perspective. For example, it poses an aviation hazard [62]. High altitude autonomous flight is being increasingly proposed for commercial ventures in the form of High-Altitude Pseudo-Satellite, High-Altitude Platform Station (or generally HAPS aircraft) which can provide communication and remote observation capabilities at relatively low cost [33]. However, in the stratosphere the density is so low that these aircraft are flying at the edge of flight capability and, although most of the turbulence is confined to the troposphere, any encounter with clear air turbulence can pose significant hazards to these small uncrewed aerial systems. Therefore, enhancing our knowledge of the turbulence in the stratosphere, and developing systems which can detect the presence of nearby turbulence in the surrounding air can help mitigate its impact.
Aviation safety is only a single example of numerous applications where atmospheric turbulence at high altitudes is important. For example, it also plays an important role in impacting electromagnetic and visible light transmission through the atmosphere, and is an important contributor to the transport of mass and momentum between the troposphere and stratosphere. Therefore, enhancing our knowledge of the turbulence in the stratosphere, and developing systems which can detect the presence nearby turbulence in the surrounding air can help mitigate its impact.

1.1 Turbulence

Turbulent flows are a phenomenon that can be visualized in many aspects of daily life, everywhere from in stirring coffee, the rushing of a river, the exhaust from a car, or the clouds of fine dirt that billow up in the wind when disturbed.

Turbulence, in general, lacks formal definition [69], but has certain properties including being composed of highly unsteady, three-dimensional, and chaotic velocity

fluctuations. Turbulence has also been found to have the following properties [51]: it is highly diffusive (effectively mixing mass, momentum and energy); very chaotic (not purely random); highly rotational and three-dimensional (composed of a range of scales of vertical structures or, informally, eddies); and strongly dissipative through the influence of viscosity (which enables energy conversion from turbulent kinetic energy to internal energy through viscous shear stresses).

Turbulence is typically produced in the form of large-scale eddies, with the scale of these eddies characterized by the boundary conditions. These eddies break down through nonlinear interactions to transfer the kinetic energy to increasingly smaller scales at which the dissipation of energy can occur through the actions of viscosity. This process is commonly referred to as the energy cascade, and is a characteristic of all turbulent flows, whether in engineering or nature [17].

1.2 Atmospheric Turbulence and its Detection

One example of turbulence that affects human life on a larger scale is the turbulence in the atmosphere. Due to its diffusive nature, turbulence plays a significant role in atmospheric transport of, for example, thermal energy, moisture, and aerosols. Hence, it is important in the interaction between the atmosphere and Earth's surface [63].

There are two primary sources of turbulence production in the atmosphere: the mechanical production of turbulence by mean velocity shear in the wind; and buoyant production resulting from convective motion [79]. Most of the turbulence exists in the troposphere, the portion of the atmosphere 6 to 10 km from the surface, which contains most of the weather phenomena. The troposphere is the lower boundary of the stratosphere, which itself is generally stable due to the inversion of the temperature gradient relative to the troposphere, caused by ultraviolet heating of the air by the sun [64].

Despite the stable nature of the stratosphere, turbulence can still occur in this cloudless atmospheric layer due to mechanical or thermal disturbances [59], and is thus often referred to as clear air turbulence. Clear air turbulence has been studied since the early 1900s, but as the aviation industry grew, it's study gained in importance [25]. There are several potential causes of clear air turbulence. For example, the horizontal movement of air above terrain (e.g. mountains) can result in upward vertical motions, shear and turbulence production within their proximity [22]. These motions are usually in the form of mountain waves (or lee waves) produced over

the mountains by wind shear and their strength is determined by the height of the mountain and the strength of the wind [78]. Another source of clear air turbulence is the presence of a jet stream [21]. Jet streams generally occur at the tropopause (the boundary region between the troposphere and stratosphere) and are a product of temperature gradients within the surrounding air [19].

Identification of the presence of atmospheric turbulence is a crucial piece of information for aviation safety. Even though most aircraft fly above the tropopause where there is limited convective turbulence, aircraft can still experience clear air turbulence which, if severe enough, can be very dangerous and has been known to cause in-flight injury of passengers and crew [21]. There are various methods used to measure turbulence in the atmosphere [74, 26, 34, 4, 31], although most studies take place in the troposphere due to the prevalence of turbulence in this layer of the atmosphere. That said, there have been several attempts at turbulence measurements in the stratosphere through weather balloon measurements, including those employing infrasonic microphones [23, 57], with some studies dating back to 1964 [74]. Some of the methods used to investigate atmospheric turbulence are discussed in the next section.

1.3 Atmospheric Turbulence Measurement

Throughout history, many technologies have been used to measure turbulence. Recently, remote sensing techniques such as lidar [13], radar [76] and sodar [72] have become increasingly used for lower altitude measurements from fixed-installations. For wide-area coverage, satellites are also employed to detect conditions which may produce turbulence [67]. These remote-sensing instruments complement in-situ sensors such as sonic anemometers [13, 72, 35], hot-wire anemometers [16, 50], multi-hole pressure probes [53, 15, 2], infrasonic microphones [20, 23, 14], hot-film probes [47], etc. which can be mounted on a mast for long-term measurement of turbulence statistics [5, 32], or can be mounted on a moving platform such as a weather balloon [14, 55, 61] or aircraft [9, 11, 77, 53, 38, 7, 3, 44, 40] for the measurement of distributed properties over a larger range of distance and higher altitudes.

In more recent studies of atmospheric turbulence in and within boundary layer (the region of the troposphere nearest the Earth's surface), uncrewed aerial systems (UASs) have proven to be very effective tools for carrying in-situ sensors (e.g. hot-wire anemometers [50], sonic anemometers [56], hot-film probes [47], multi-hole pressure probes) [77]. Many of the UAS used for turbulence study use multi-hole probes

[71, 3], which measure the dynamic pressure of the air, with multiple stagnation pressure ports combined with a directional calibration used to determine the wind vector relative to the probe axis. Due to their fragility, hot-wire probes, which measure the convective heat transfer across a very thin heated filament, are usually reserved for short-term scientific studies [60]. However the fast response of the hot-wire anemometer allows detailed characterization of the turbulence, for example allowing the measurement of small-scale fluctuations corresponding to turbulent dissipation [6, 8].

A sonic anemometer is also an in-situ sensor which can be mounted on a tower or be placed on a UAS [7, 10, 39, 49]. Although a sonic anemometer does not have the time-response to match a hot-wire anemometer, or even a multi-hole probe, its lack of moving parts and ability to resolve all three components of the wind vector make it ideal for long-term studies [46].

One ground-based remote sensing technique used to measure turbulence and vertical wind profiles from close to the surface up to a few hundred meters above ground, is sodar (sound detection and ranging) [72]. By emitting audible range acoustic pulses, the portion of the signal that is back-scattered due to the atmosphere's refractive index can be measured. Variations in the refractive index which occur as a result of turbulent fluctuations can be identified by a sodar via processing of the back-scattered signal and producing a Doppler spectrum. However, there are limitations to using sodar for measuring turbulence due to attenuation effects, as well as a lack of ability to perform spatial sampling [73].

Radar (radio detection and ranging) is based on a concept similar to sodar but in this case the radio domain of the electromagnetic waves are transmitted and the reflected wave is received and processed to determine the speed and the distance of the medium [76]. Radars can effectively work on aircraft or be used as ground-based sensors. Although typically used for measuring moisture content, The National Center for Atmospheric Research has developed a turbulence detection algorithm which is able to produce eddy dissipation rate estimates from input parameters of the Doppler spectrum (reflectivity, radial velocity and spectrum width) [76]. Although the focus of this work was on convective turbulence and thunderstorm evolution the maps produced by their algorithm can potentially be read and observed by pilots and airline dispatchers.

A frequently used sensor with a variety of applications, ground based or airborne, is lidar (light detection and ranging). Lidar is another ranging remote sensing instrument using an emitter and detector to use changes in the reflected signal to discern

details about the environment, although lidar use different light wave ranges [43]. Although capable of measuring turbulent kinetic energy, turbulence intensity, and stress velocity turbulence intensity, this method is unable to measure shear velocity accurately [13].

Weather balloons assist in-situ measurement of turbulence and weather conditions in general [28]. Sensors can be mounted on the weather balloons which can rise up to middle atmosphere (about 40 km). Radiosonde sensors are able to measure characteristic weather properties(temperature, pressure, relative humidity) as it rises. They also send data back to ground stations which include balloon location which can be used to calculate wind velocity data. Infrasound sensors are also employed on weather balloons to detect upper air phenomena such as gravity waves which are themselves a source of turbulence [14].

Satellites are popular for remote sensing of atmospheric conditions, but are not yet able to measure winds or turbulence directly. Instead they are used to infer the potential for the formation of turbulence based on atmospheric conditions.

Finally, relevant to the present research, several previous studies have experimented with the use of infrasonic microphones on weather balloons to detect stratospheric turbulence [14, 74]. However, there have not been any experiments done by placing these microphones on aircraft for local detection.

1.4 Research Objective

One of the biggest impacts of turbulence is on the aviation safety, however, there are other consequences of the disturbances induced by atmospheric turbulence at high altitudes that motivate its study. For example, the density variations introduced by atmospheric turbulence can affect ground-satellite inter-communication. Signal attenuation and frequency shift due to turbulence (ray bending) can negatively affect the strength of the signal at the receiver [18]. Such disturbances do not only affect radio communication, but also optical communications as well. In free-space orbital communications, irradiance induced by turbulence is a major challenge due to its attenuation of laser signals, impacting signal-to-noise ratio [37]. In addition to these commercial applications, stratospheric turbulence can impact momentum transfer and the dispersion of scalars, as exemplified by wild-land fire smoke, which can transport long distances and has potentially significant health impacts [24].
In order to achieve the fullest commercial use of high altitudes it is essential to identify and detect clear air turbulence precursors, particularly for lightweight UAS which

may be serving as in-situ low-orbit satellites. Currently, there are significant gaps in the development of forward-sensing turbulence detection [57]. This research examines potential turbulence detection strategies for high altitudes using light-weight, compact, low-cost sensors integrated on a small UAS. To this end, this work examined two approaches via a collaboration between the University of Kentucky and NASA Langley Research Center, the first approach using UAS the signals from aircraft-borne wind sensors and the second utilizing infrasonic acoustic signatures to remotely detect the presence of turbulence which will not be discussed here.

These two sensors were tested in 2021 by conducting three high-altitude flight tests at Spaceport America in New Mexico USA, reaching peak altitudes of 25 km to 30 km. This was accomplished by utilizing a balloon-launched UAS in the form of a stratospheric glider, the HiDRON H2 aircraft operated by Stratodynamics. The glider offers the advantage over traditional balloon launches by being able to maximize time at altitude during its descent phase, thereby facilitating the statistical analysis required for turbulence detection.

The following chapters first provide a background and literature review (Chapter 2) and describe the experiment in detail (Chapter 3), with Chapter 4 providing an overview of the results and analysis, specifically the ambient conditions during each flight and in-situ measurements of atmospheric properties, including a description of where turbulence was identified. Finally, a summary of conclusions and discussion of potential future work is provided in Chapter 5 .

Copyright© Anisa Haghighi Najafabadi, 2023.

Chapter 2 Background

Numerous approaches have been developed to describe fluid flow and its turbulent behavior [51]. The equations of motion for a fluid flow appear in the form of partial differential equations; the Navier-Stokes equation coupled with conservation of mass and energy. Although these equations have been demonstrated to be accurate models, their analytical solution is intractable and their numerical solution is limited to low Reynolds numbers [48]. Hence, statistical approaches and empirical observation have become important contributions to understanding turbulent behavior and introducing simplifying models and assumptions that can be used to facilitate their numerical solution [29].

Despite over a century of work in this area, predicting the presence and characteristics of turbulence in the atmosphere is still a significant challenge [52]. Hence, when trying to identify the presence of turbulence, observations via measurement are still necessary. This means that the inherent signatures of turbulence, such as its acoustic noise generation, can be valuable markers for identifying the presence of turbulence. Furthermore, a dynamical systems approach using historical flow velocity data to solve a multi-dimensional Navier-Stokes approximation can also offer key markers to indicate the incipient transition to turbulence.

2.1 Navier-Stokes Equation

For most of the lower atmosphere, the velocity field is well described using the Navier-Stokes Equation, an expression of the linear momentum equation which, for an incompressible, Newtonian fluid, appears as

$$\rho \frac{DU_i}{Dt} = -\frac{\partial p}{\partial x_i} + \rho g_i + \mu \frac{\partial^2 U_i}{\partial x_j \partial x_j}, \tag{2.1}$$

where D/Dt indicates a total derivative, $\partial p/\partial x_j$ is the pressure gradient $\vec{g} = g_i \vec{e}_i$ is the local gravitational vector, $\vec{U} = U_i \vec{e}_i$ is the local velocity vector, ρ is the air density and μ its dynamic viscosity. Here, the summation notation is used and vector quantities appear through their components, e.g. U_i are the components of the velocity vector corresponding to the Cartesian base vectors $\vec{e}_i$.

When combined with the conservation of mass equation for incompressible flow

$$\frac{\partial U_i}{\partial x_i} = 0, \tag{2.2}$$

the result is a closed system of equations which can be solved for isothermal flows. Note that the assumption of incompressibility in the atmosphere is not strictly valid due to the vertical density gradients. However, it is common practice to implement the Boussinesq approximation [64] in that density variations can be approximated as a variation about a fixed local density, ρ_0. Assuming the variable density, ρ, is only important in the gravitational term, then local density variation due to temperature can be introduced into the Navier-Stokes equation as

$$\frac{DU_i}{Dt} = -\frac{1}{\rho_0}\frac{\partial p}{\partial x_i} + \frac{\rho}{\rho_0}g_i + \nu\frac{\partial^2 U_i}{\partial x_j \partial x_j} - g_i\alpha(T - T_0). \tag{2.3}$$

If one now considers a hydrostatic pressure variation due to altitude such that $\frac{\partial \overline{p}}{\partial x_3} = -\overline{\rho}g_3$ (assuming g_3 is the direction normal to the Earth's surface) such that the overbar indicates the hydrostatic component, then pressure can be written as $p = \overline{p} + p'$ and density can be written as $\rho = \overline{\rho} + \rho'$. The Navier-Stokes equation then is further altered to

$$\frac{DU_i}{Dt} = -\frac{1}{\rho_0}\frac{\partial p'}{\partial x_i} + \frac{\rho'}{\rho_0}g_i + \nu\frac{\partial^2 U_i}{\partial x_j \partial x_j} \tag{2.4}$$

If a linear dependence on temperature is assumed such that

$$\rho' = -\alpha\rho_0(T - T_0) \tag{2.5}$$

where T is the temperature, T_0 a reference temperature corresponding to ρ_0 and α the coefficient of thermal expansion, then it is possible to recast this equation to account for density and temperature dependence with altitude as

$$\frac{DU_i}{Dt} = -\frac{1}{\rho_0}\frac{\partial(p - \rho_0 g_3)}{\partial x_i} + \nu\frac{\partial^2 U_i}{\partial x_j \partial x_j} - g_3\alpha(T - T_0). \tag{2.6}$$

Note that the temperature can be determined using the heat equation

$$\frac{DT}{Dt} = \frac{K}{\rho C_p}\frac{\partial^2 T}{\partial x_j \partial x_j} + \frac{J}{\rho C_p}. \tag{2.7}$$

Here ρC_p is the heat capacity per unit volume, K is the thermal conductivity and J is the rate per unit volume of internal heat production.

2.2 Turbulent Kinetic Energy

Although turbulent behavior can be captured by the Navier-Stokes equation, its chaotic behavior in time and space result in a largely statistical description being

used to characterize it [66]. Key to understanding the magnitude of turbulence at a point in space is the turbulent kinetic energy, defined as

$$k = \frac{1}{2}\langle u_i u_i \rangle = \frac{1}{2}(\langle u_1^2 \rangle + \langle u_2^2 \rangle + \langle u_3^2 \rangle) \tag{2.8}$$

where u_i are the fluctuating components of the velocity vector, themselves defined through a process referred to as Reynolds averaging whereby

$$u_i = U_i - \langle U_i \rangle. \tag{2.9}$$

Here the angle brackets, $\langle\ \rangle$, indicate an average; either a time average or ensemble average depending on the process. The rate of change of k at a location in space is dependent on the balance between rates of turbulent production, transport, viscous diffusion and viscous dissipation.

A turbulent kinetic energy transport equation can be derived in which the time rate of change of turbulence at a point in space is composed of a balance of turbulence production due to shear and buoyancy effects, advection from other locations, correlation between pressure and velocity fluctuations, and dissipation due to viscous effects, ε. It is common to assume a stationary, homogeneous turbulence field where the production terms balance the dissipation terms. In these conditions, this turbulent kinetic energy dissipation rate can also be a measurement for the turbulence intensity.

2.3 Turbulent Kinetic Energy Dissipation Rate

Turbulent eddies at small-scales are subject to dissipation by viscous stresses, even at the highest Reynolds numbers. The dissipation rate of the turbulent kinetic energy is given by

$$\varepsilon = \frac{1}{2}\nu \left\langle \left(\frac{\partial u_i}{\partial x_j} + \frac{\partial u_j}{\partial x_i}\right)\left(\frac{\partial u_i}{\partial x_j} + \frac{\partial u_j}{\partial x_i}\right) \right\rangle \tag{2.10}$$

where $\nu = \mu/\rho$ is the kinematic viscosity. As noted above, the dissipation rate plays an important role in the kinetic energy balance of turbulence and in the scaling of the energy spectrum of turbulence.

2.4 Energy Spectrum of Turbulence

Turbulence is a multiscale phenomena, consisting of a range of scales at which the turbulent motions exist. Hence, turbulence is frequently analyzed by examining the

spectrum of its turbulent kinetic energy as a function of either space (through the wavenumber vector $\vec{\kappa}$ or its magnitude κ) or time (through frequency, f).

The energy spectrum of turbulence is characterized by a cascade of kinetic energy from large to small scales. In this energy spectrum, the largest scales of turbulence (i.e. the energy containing range) are fed kinetic energy by the turbulent production mechanism (e.g. shear or buoyant production). Kolmogorov [42] theorized that a universal equilibrium range of wavenumbers would exist at the smaller scales of turbulence. At the very smallest scales of turbulence it is subject to viscous forces, forming the dissipation range. It is in this range that the kinetic energy dissipates to thermal energy at a rate equal to ε. Hence, in the dissipation range, the energy spectrum scales on both ν and ε.

In relatively high Reynolds number flows, such as the atmosphere, an inertial subrange of the kinetic energy spectrum also forms. In this range of scales the eddies are smaller than the energy containing eddies, and hence no energy is added from production. In addition, these eddies are too large and energetic to be subject to viscous dissipation. Thus range, lacking neither production nor dissipation mechanisms, transfers energy inertially to the dissipation range at a rate equal to ε, and hence in this range the energy spectrum scales only on epsilon. This property leads to what is referred to as Kolmogorov's $-5/3$ law, which says that in the inertial subrange the three-dimensional wavenumber spectrum, $E(\kappa)$, will follow power-law scaling such that

$$E(\kappa) = C\varepsilon^{2/3}\kappa^{-5/3} \tag{2.11}$$

where C is an arbitrary constant referred to as the universal Kolmogorov constant.

Using the Kolmogorov $-5/3$ law, in combination with semi-empirical descriptions for the energy containing and dissipation ranges, a simple model spectrum can be built. As described by Pope [51], this model spectrum takes the form

$$E(\kappa) = C\varepsilon^{\frac{2}{3}}\kappa^{-\frac{5}{3}} f_L(\kappa L) f_\eta(\kappa\eta). \tag{2.12}$$

Here, the scales L and $\eta = (\nu^3/\varepsilon)^{1/4}$ describe the scale of the energy containing eddies and dissipative eddies respectively. Equation 2.12 is also known as the von Kármán spectrum [51] where the functions f_L and f_η describe the energy containing range

$$f_L(\kappa L) = \left(\frac{\kappa L}{[(\kappa L)^2 + c_L]^{1/2}}\right)^{5/3+p_0} \tag{2.13}$$

and dissipation range

$$f_\eta(\kappa\eta) = \exp(-c_\beta[(\kappa\eta)^4 + c_\eta^4]^{1/4} - c_\eta). \tag{2.14}$$

These functions scale on L and η respectively and introduce positive constants c_L, p_0, c_β, and c_η which are determined empirically [51]. These functions are defined such that at large η, $f_L \to 1$, and at small η, $f_\eta \to 1$, such that in the inertial subrange equation 2.12 converges to equation 2.11.

Note that the model spectrum defined above is for the three-dimensional scalar spectrum. For most experiments and many flows, it is more convenient to use a one-dimensional spectrum E_{11} defined along a single direction prescribed by the wavenumber vector component, κ_1. Consequently, equation 2.11 for the one-dimensional spectra is given by

$$E_{11}(\kappa_1) = C_1 \varepsilon^{2/3} \kappa_1^{-5/3} \tag{2.15}$$

where

$$C1 = \frac{18}{55} C \approx 0.49 \tag{2.16}$$

In Figure 2.1, the behavior of the above equations is demonstrated using their equivalent one-dimensional form. The inertial sub-range length varies with Reynolds number, therefore an important point to consider when analyzing turbulent flow behaviors. Note that, due to the very high Reynolds numbers which exist in the atmosphere, combined with limitations in instrumentation, the energy containing range and dissipation ranges typically not resolved and the energy spectrum often analyzed in the context of just the inertial subrange.

2.4.1 Atmospheric Gravity Waves

When a parcel of air rises, if the surrounding air is unstable (i.e. the density increases with altitude), it will continue to rise, being less dense than the surrounding air. However, if the air around it is stable (i.e. the density decreases with altitude), the parcel is forced back down, as it is more dense than the surrounding air. In the latter situations, for a strong enough displacement, this can create a cascade of motion when the parcel sinks due to its own momentum, resulting in the parcel over-correcting to a more dense surrounding. In the process of seeking an equilibrium this process can continue over large distances until viscosity can dissipate the momentum of the air parcel. The result is what is referred to as a gravity wave.

Weather fronts, jet streams, wind over mountains are potential triggers of gravity waves. Lee waves or mountain waves are categorized as internal gravity waves which occur in stratified air. One potential outcome of gravity waves is the production of clear air turbulence, of great concern for the aviation safety.

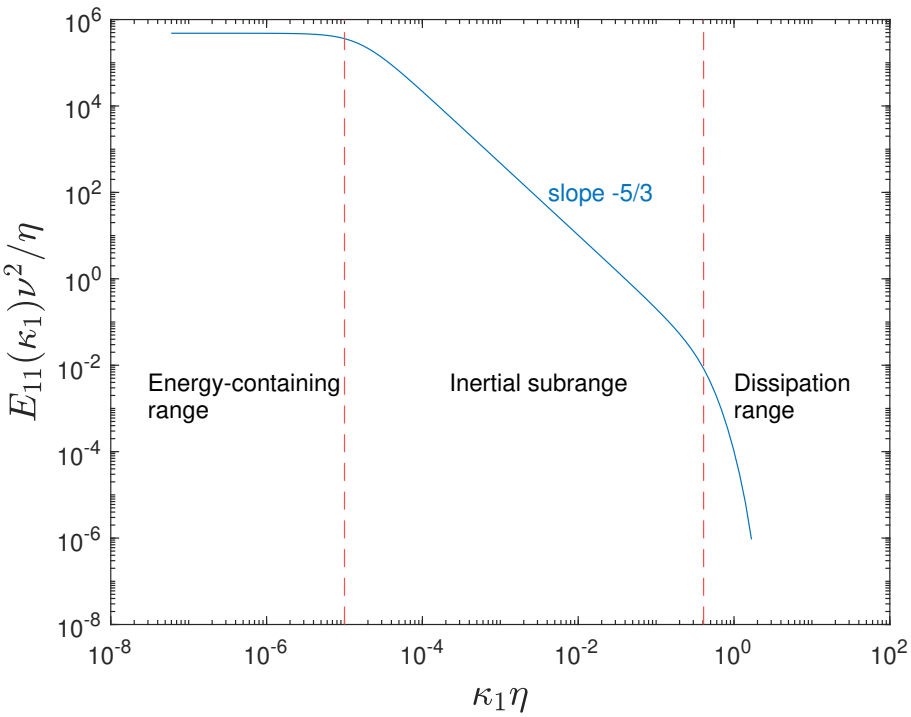

Figure 2.1: The model spectra in one-dimensional form showing the different subranges at an arbitrarily high Reynolds number.

2.4.2 Brunt-Väisälä Frequency and Richardson Number

The period of a gravity wave can reveal certain clues to its origin or generation source. A displaced parcel of air in a stratified environment will oscillate as it propagates vertically. The frequency of this oscillation is given by

$$N = \sqrt{\frac{g}{\theta_v}\frac{d\theta_v}{dz}} \tag{2.17}$$

where N is the Brunt-Väisälä Frequency, g is the local acceleration due to Earth's gravity, θ_v is the virtual potential temperature and z is the altitude. This is also referred to as the buoyancy frequency as it describes a static stability of the air compared to the convection mechanism around it. Existence of wind shear in statically stable environment has the potential to create dynamic instability and for the flow to become turbulent [64]. The ratio of the buoyancy term to the flow shear term is give by

$$Ri = \frac{N^2}{(dU/dz)^2} \tag{2.18}$$

where Ri is the Richardson number, U is the magnitude of air velocity and $z = x_3$ is the altitude or the depth of the layer. A critical Richardson number of 0.25 is defined which indicates that for $Ri < 0.25$ the flow is dynamically unstable. It is important

to note that a parcel of air has to be both statically and dynamically stable for a laminar flow, but being only statically or dynamically unstable can be a cause of turbulence.

Stability of a parcel of air depends on many environmental factors. One important parameter that can provide information about the atmospheric stability is the decrease of temperature with altitude, or lapse-rate, defined as

$$\Gamma = -\frac{dT}{dz}. \tag{2.19}$$

The dry adiabatic lapse rate is around 9.8°C km^{-1} and a moist adiabatic profile will have a lapse rate of about 6°C km^{-1}. Below 6°C km^{-1}, there will be a sub-adiabatic profile which means that temperature either stays constant with increasing altitude or the temperature will increase with altitude (called a temperature inversion). The other scenario is a lapse rate of greater than 9.8°C km^{-1}, which is called super-adiabatic, in this case the atmosphere is unstable. A value between the two is a conditionally unstable atmosphere. This conditional instability is directly influenced by the amount of moisture in the air.

2.5 In-situ Measurements of Stratospheric Turbulence

As was mentioned previously, behavior of turbulence in the upper atmosphere is important for aviation safety. Hence, many experiments have studied turbulence measurement in the stratosphere using balloon-borne instruments. Due to its relationship to the scaling of the inertial turbulence (e.g. through equation 2.11) and hence the kinetic energy in the upper atmosphere, an important parameter is the turbulent kinetic energy dissipation rate, ε. However, there are various methods used to measure it, each with their own limitations. For example, response time of the instrument has to be sufficiently high to resolve the high-frequency small-scale motions with corresponding requirements for the instrument's spatial resolution.

Previously published studies of stratospheric turbulence date back to 1960s [27], typically employing instruments mounted on balloons [74, 26, 34, 14]. Amongst the relevant conclusions from these studies were that stratospheric turbulence tends to form in relatively thin atmospheric layers due to intrinsic static stability at these altitudes. These previous studies have also identified instances of high turbulent kinetic energy dissipation rate which were compared to Richardson number to determine a convective or mechanical source of turbulence [65, 58, 41] and used to model the relationship between turbulence in upper atmosphere and tropospheric activity [20].

In early 2010s, the Leibniz-Institute Turbulence Observations in the Stratosphere (LITOS) experiment was conducted in which balloon experiment campaigns were performed to measure characteristics of turbulence layers in the stratosphere using a temperature anemometer to measure velocity fluctuations. The obtained measurements of wind and temperature measurements were within sub-centimeter resolution, and therefore suitable for resolving the finer scales of turbulence. This experiment reached altitudes up to 30 km, and the dissipation rates were then compared to the square Brunt-Väisälä frequency (N^2) and the Richardson number (Ri) as a function of altitude. Turbulent layers with various thicknesses were selected to perform a more detailed comparison. The energy dissipation rates seemed to increase with altitude and there was a clear correlation between turbulent events and $Ri < 1/4$. However, in some instances turbulent events were also observed where $Ri > 1/4$. Though there are numerous experimental studies that confirm $Ri < 1/4$ signifies existence of turbulence, more and more studies are finding that turbulence can survive where Richardson number is far greater that unity. Also, if sufficiently small scales (relative to the turbulent layer thickness) are considered when calculating Ri, a critical Richardson number (i.e. $Ri = 1/4$) may be observed [34].

In the winter of 2020, in order to provide a more detailed and quantitative explanation of lower stratosphere turbulence, LITOS was launched again on a balloon using a temperature anemometer capable of measuring velocity fluctuations. The objective was to detect the presence of breaking Rossby waves (planetary waves) induced by the jet stream and to study the developed tropopause fold to calculate the energy dissipation rate. Tropopause folds occur when air from lower stratosphere sinks below the jet stream, and there is a corresponding vertical movement of trace gases (tropopause folds are especially important because they tend to intensify turbulence and create aviation safety concerns) [65]. In order to measure the dissipation rate, a fit of the power spectral density was performed within the inertial and viscous subrange using slopes $-5/3$ and -7, respectively. This fitting method has its own limitations and need to satisfy certain criteria for validation [65]. Using the fit values the dissipation rate was then calculated by

$$\varepsilon = c_{l0}^4 \frac{\nu^3}{l_0^4} \tag{2.20}$$

where $c_{l0} = 15.8$ was unique to the measurement geometry of the experiment, and l_0 is the Taylor micro-scale.

The observational result was that dissipation rates above the jet stream (lower stratosphere) were three orders of magnitude larger than below the jet stream (upper

troposphere). In a deep tropopause fold case, severe turbulence values were observed although the turbulence scale was moderate in medium-fold cases. The lower stratospheric measured dissipation rate seemed consistent with lower Richardson numbers.

In 1995, an in-situ turbulence detection algorithm was developed by NCAR and implemented on some 200 aircraft. A turbulence intensity metric developed was the cubic root of kinetic energy dissipation rate. Referred to as the eddy dissipation rate

$$EDR = \varepsilon^{1/3}, \tag{2.21}$$

it is currently being used as a standard turbulence reporting metric by the International Civil Aviation Organization (ICAO). In the NCAR study the EDR values were calibrated for different aircraft types with the obtained values of pilot reports (PIREPs) for optimization. The EDR calculation algorithm uses the von Kármán energy spectrum model (equation 2.11) along with either vertical-wind-based algorithms or the aircraft's response time to vertical acceleration, each implemented on a different aircraft. The results when compared to PIREPs yielded a quadratic relationship between the two, which can later be calibrated for different aircraft sizes and models. This comparison revealed that the current ICAO scale of EDR for turbulence intensity may be higher than experimental results. Additionally, a comparison of the two methods of the measurement was also included showing they are consistent (at least for medium-sized aircraft) [58].

Copyright© Anisa Haghighi Najafabadi, 2023.

Chapter 3 Experiment

To assess the viability of using a balloon-launched autonomous glider for detailed atmospheric measurements, a one-week measurement campaign was conducted in which the HiDRON H2 glider was instrumented with instruments capable of measuring pressure, temperature, humidity, wind speed and direction as well as infrasonic sound levels. This chapter provides a description of the measurement campaign, aircraft, sensor payload and the procedure used to extract wind vectors from the raw data are provided below.

3.1 Overview

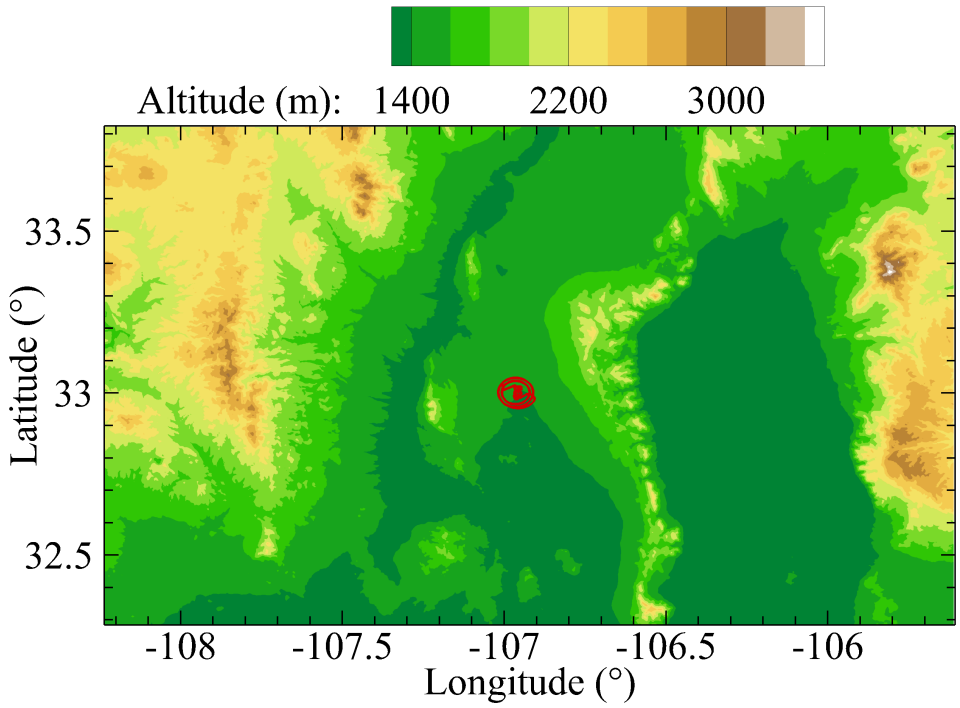

Figure 3.1: The topography of the flight area with Spaceport America with the area encompassed by the flight indicated by a white circle.

The flight campaign was conducted at Spaceport America near Truth or Consequences, New Mexico (Figure 3.1) from June 1, 2021 through June 6, 2021 to assess the sensors' ability to detect turbulence. Secondary objective entering the campaign was to obtain flight data, and demonstrate operability of the sensors at 25,000 m (80,000 feet) AGL. Three flights were flown with Flight 1 being conducted on June

1, Flight 2 conducted on June 4 and Flight 3 being conducted on June 6. The flight provider, Stratodynamics, successfully reached 25,000 m altitude for Flights 1 and 2, and reached an altitude of 30,000 m (100,000 feet) AGL on Flight 3.

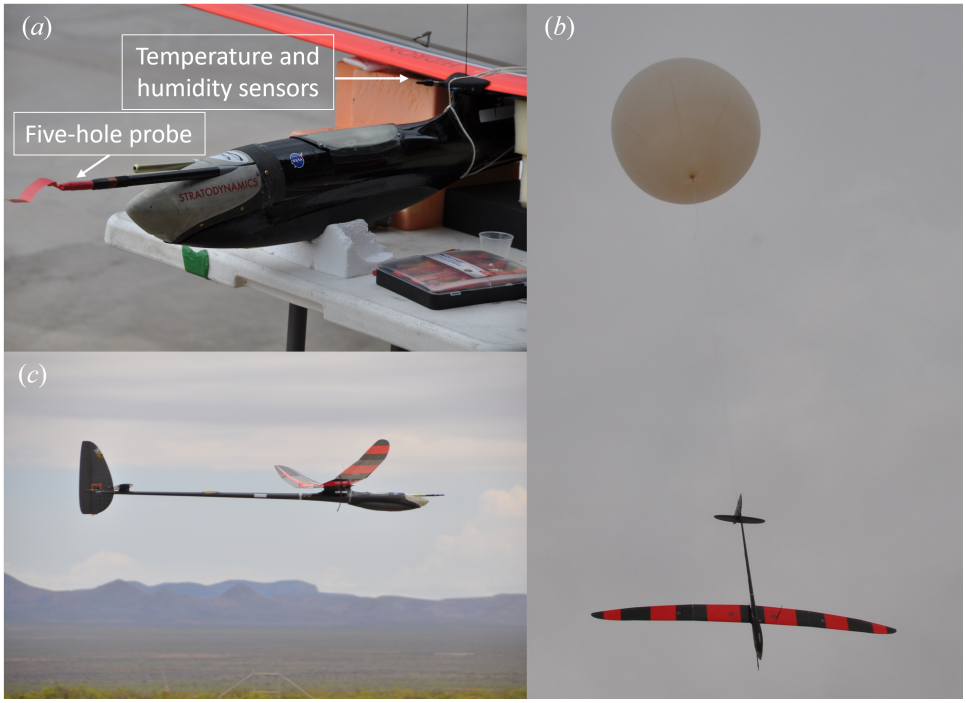

Figure 3.2: Images of HiDRON H2 showing: (*a*) close up of aircraft nose showing five-hole probe and temperature and humidity sensor location; (*b*) aircraft during launch; and (*c*) aircraft during landing.

3.1.1 Aircraft

Key to the research was the use of the host UAS platform, the HiDRON H2 (see Figure 3.2), operated by flight provider Stratodynamics Inc. The HiDRON H2 is a balloon-launched carbon fiber/fiberglass glider UAS that is capable of autonomous and soaring flight modes. It has a wingspan of 3.8 m and its nominal flight weight is approximately 5.7 kg with the payload. To achieve initial altitudes in excess of 30 km, the HiDRON H2 is launched using latex sounding balloons. After release, the aircraft follows a pre-programmed descent pattern towards a planned landing point. An operator tracks the HiDRON H2 position from launch to landing through a portable ground station. Changes to the flight plan can be made in real time through radio telemetry which also allows operational parameters to be transmitted to the ground with a range of 100 km. Other safety features include a parachute, dual-redundant balloon release system and geofencing safety protocols that prevent the aircraft from

leaving the designated airspace. During prior flights, including flights exceeding altitudes of 30 km, the HiDRON H2 has shown reliability in remaining controllable in high-wind (as high as 32 m s^{-1}), operating in low-temperature conditions ($< -60°C$), and in returning to a predefined landing site.

For this flight operation, the autopilot was set to maintain the aircraft's kinetic energy (reflected through the indicated airspeed), with the value selected near the optimal lift over drag ratio (the maximum distance that can be travelled per loss in altitude). To maintain the set airspeed the autopilot adjusts the pitch angle on the elevator to control the angle of attack of the main wing airfoil. The horizontal velocity is a result of setting the airspeed and may fluctuate slightly due to the pitch angle adjustments. Also, as the aircraft descends in altitude the air density increases and the HiDRON's aerodynamic performance improves; thus, the horizontal velocity gradually decreased as the aircraft descended. Figure 3.3 shows the horizontal speed, $|\vec{V}_G|$, and descent speed relative to the ground, as well as the magnitude of the aircraft's velocity relative to the wind, $|\vec{V}_R|$, for each of the three flights. The relative horizontal velocity magnitude was found from $|\vec{V}_R| = ((V_{G_X} - u_1)^2 + (V_{G_Y} - u_2)^2)^{1/2}$ where (V_{G_X}, V_{G_Y}) are the horizontal velocity components of the aircraft relative along the ground to the East and North respectively and (u_1, u_2) are the corresponding horizontal velocity components of the wind, with the method used to obtain the wind velocity vector provided in the next section.

To measure ambient conditions, the aircraft is equipped with an InterMet Systems iMet-XF system having fast response bead thermistor air temperature and humidity sensors.

Full telemetry information at a 10 Hz was provided by Stratodynamics Inc. for all three flights, which included position, ground speed, 6 degree-of-freedom orientation information and pressure, temperature and humidity information from the iMet-XF sensors.

3.1.2 Payload

The payload operated by the University of Kentucky was a combination of four components: (1) five-hole probe; (2) infrasonic sensor; (3) data acquisition board; (4) embedded computer. These basic payload components were installed in the nose of the HiDRON H2, which could be accessed via removal of the nose cone, as shown in Figure 3.4.

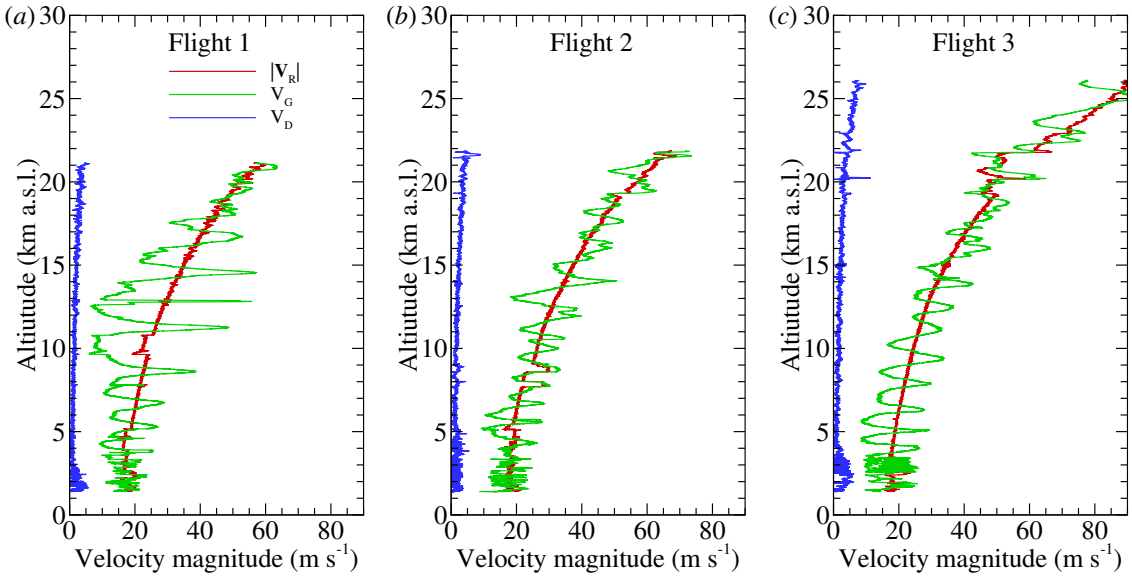

Figure 3.3: Horizontal ground speed in inertial Earth-fixed coordinates, $|\vec{V}_G|$, magnitude of the descent speed in inertial Earth-fixed coordinates and relative air velocity magnitude in aircraft-fixed coordinates, $|\vec{V}_R|$, for (a) Flight 1, (b) Flight 2 and (c) Flight 3.

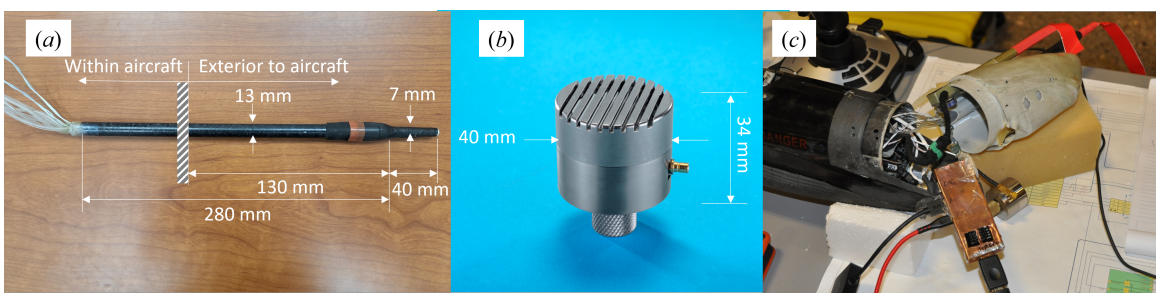

Figure 3.4: (a) Five-hole probe, (b) infrasonic microphone, and (c) nose payload bay open between flights, with embedded computer shown removed for data retrieval. Infrasonic microphone is below embedded computer but was installed in aircraft nose facing forward during flight.

Five-Hole Probe: Wind speed and direction relative to the aircraft was measured using a five-hole probe. The probe, shown in Figure 3.4a, is a carbon-fiber tube equipped with a beveled aluminum tip. The tip is arranged with one center hole normal to the probe axis surrounded by four other holes arranged symmetrically around the center hole with their plane normal vector aligned 20° to the probe axis. For this measurement, the pressure difference between central hole (measuring total stagnation pressure) and a series of additional holes arranged on the carbon fiber tube (measuring static pressure) were used to determine the approximate dynamic pres-

sure at the probe tip. The pressure difference between the two horizontally-aligned circumferential holes are arranged to produce a pressure difference which changes with the horizontal angle of the wind vector relative to the probe axis. Similarly, the two vertically-aligned circumferential holes are arranged to produce a pressure difference which changes with the horizontal angle of the wind vector relative to the probe axis. Prior to installation on the HiDRON, the probe was calibrated in a wind tunnel using an apparatus designed to pitch and yaw the probe at angles up to 25° relative to the mean wind vector.

Based off of established procedures, e.g. as outlined by Treaster and Yocum [68], Wildmann et al. [75], Bohn et al. [12] and Kroonenberg [70], the pressure differences at each yaw and pitch angle combination were used to build pressure coefficients

$$C_\beta = \frac{\Delta P_{32}}{\Delta P_1 + 0.5(\Delta P_{32} + \Delta P_{54})} \tag{3.1a}$$

$$C_\alpha = \frac{\Delta P_{54}}{\Delta P_1 + 0.5(\Delta P_{32} + \Delta P_{54})} \tag{3.1b}$$

$$C_q = \frac{\Delta P_1 - Q}{\Delta P_1 + 0.5(\Delta P_{32} + \Delta P_{54})} \tag{3.1c}$$

where ΔP_1 is the pressure difference between the central hole and the static pressure, ΔP_{32} is the pressure difference across the horizontal probe holes, ΔP_{54} is the pressure difference across the vertical probe holes and Q is the dynamic pressure of the wind tunnel. The probe design results in unique combinations of C_α and C_β for each yaw and pitch angle of the probe relative to the wind vector. To analyze the flight data, C_α and C_β are calculated for every measurement point and the unique combination used to determine the wind vector angle relative to the probe axis. The corresponding value of C_q measured at that relative angle is then extracted from the calibration data, allowing Q to be determined from the measured ΔP_1. The result is knowledge of the magnitude and direction of the dynamic pressure vector relative to the probe axis. This is then converted to velocity using the density determined from measurements of the ambient pressure, temperature and humidity.

The probe used on these flights was also heated to prevent ice forming on in the probe during flight. This was accomplished by wrapping the probe body in nickel Chromium resistance wire. A feedback circuit, using a thermistor attached to the probe tip, passed current through the wire at a rate sufficient to maintain the probe tip temperature at 50 °C. Comparison of calibrations with and without heating active indicated no influence of probe heating on the five-hole-probe directional response characteristics.

Each hole was connected to differential pressure transducers through 1.75 mm diameter Tygon tubing. To ensure that the low density conditions at flight altitude did not result in pressure differences below the sensitivity of an individual transducer each ΔP_1, ΔP_{23} or ΔP_{45} pressure difference was converted to analog voltage using two different transducers. The low sensitivity transducer was a TE Connected Measurements 4515-DS5A002DP differential pressure transducers with a 500 Pa range. The second transducer was an Allsensors DS-0368 differential pressure transducer with a 65 Pa range. Both sets of analog output voltages were linearly scaled relative to the maximum transducer range with a nominal span of 4.5V and 4.0V respectively. Note that during flight, the autopilot maintained nearly constant dynamic pressure within the range of the low-sensitivity transducers and hence only the readings from these sensors were used.

To convert the velocity vector magnitude and direction relative to the probe axis into a frame of reference relative to the ground, an additional coordinate transformation was conducted using the aircraft's pitch, yaw, and roll angles as measured by the autopilot. Details of this process are provided in [77] and are based off of procedures described in [45] for measurements using similar probes mounted on crewed aircraft. An additional estimate and correction of the misalignment of the probe axis and aircraft's body-frame axis, airframe influence on the probe, and time misalignment between sensors, was conducted following the approach described in [2]. The resulting time-dependent wind velocity vector is described using components $u_1(t)$, $u_2(t)$, and $u_3(t)$ which are aligned to the East, to the North, and up, respectively. The time-dependent horizontal wind velocity magnitude and direction were then found from

$$U(t) = \left(u_1(t)^2 + u_2(t)^2\right)^{-0.5} \tag{3.2}$$

and

$$\gamma(t) = \text{atan2}\left(-u_1(t), -u_2(t)\right) \tag{3.3}$$

where atan2 indicates a numerical implementation of the $\tan^{-1}$ function used to disambiguate the polar direction using the quadrant formed by the sign of the velocity components.

As the autopilot and payload data acquisition systems were acquired asynchronously, alignment of autopilot kinematic data and five-hole-probe pressure data in time was conducted during post-processing by cross-correlating the dynamic pressure measured by the aircraft's intrinsic pitot probe (recorded by the autopilot along with the air-

craft position and orientation information) and the dynamic pressure measured by the difference between the central port of the five-hole probe and the static pressure ports (recorded by the payload data acquisition system). The time lag between the two systems was then removed before performing the transformation of the velocity vector in the aircraft body frame to the Earth-fixed frame of reference. To do so, the aircraft position and orientation information was up-sampled from the autopilot's 10 Hz sample rate to the 1 kHz sample rate used by the on-board data acquisition system, with the up-sampling conducted using simple linear interpolation. Note also that, although data was acquired at a 1 kHz sample rate, the actual probe frequency response was estimated to be on the order of 20 Hz using the same measurement approach utilized in [77], which measures the response of the system following a step change in pressure. The limitation in frequency response is caused by viscous attenuation of the pressure fluctuations within the tubing, coupled with inaccuracies introduced by high-frequency resonance within the transducer cavity.

Finally, it should be mentioned that a pressure line was inadvertently disconnected during maintenance prior to Flights 2 and 3, requiring the conversion of five-hole probe voltages to wind for these flights to take a slightly different approach. For these flights, the calibration was updated such that C_α was set to zero and the data processed without the missing transducer. As C_α has primary importance in determining the pitch angle of the flow relative to the probe axis, this value was replaced using the angle of attack determined by the aircraft's autopilot, specifically the angle between the true airspeed determined from the aircraft's pitot probe, and the vertical velocity determined by the aircraft's variometer. To verify that this approach was justified, the Flight 1 data was processed with the original and revised approach, and the impact on the resulting wind velocity statistics found to be negligible, although some differences in the frequency content of the vertical wind component could be expected.

Infrasonic Microphone: A property of infrasound particularly favorable to the objectives of the proposed work is that it propagates over long distances (hundreds of kilometers) with little attenuation. Hence, infrasonic measurements (measurements of acoustic frequencies below 20 Hz) were conducted using an infrasonic microphone. For these tests an extremely low frequency (ELF) microphone and acoustic measurement system developed by Dr. Qamar Shams' group at NASA Langley Research Center (LaRC) was used. Note that, although these sensors are sufficiently compact for usage on a UAS, this was the first implementation of this system on one. This

microphone was capable of infrasound detection in a portable and easily deployable from factor with a sealed backchamber to allow substantially no air exchange between the backchamber and outside the microphone. The location and sizes of the holes, the size of the slot, and the volume of the backchamber were selected such that membrane motion was substantially critically damped and optimally dimensioned for the 0.01-20 Hz frequency range. A signal conditioning unit provided by LaRC amplified the microphone output to a ± 10 V full-scale output.

Data Acquisition: A Measurement Computing Systems MCC USB-1608FS-Plus data acquisition system (DAQ) was used to digitize the voltage output from the six pressure transducers and microphone signal conditioning unit. This particular unit is capable of recording 8 single-ended analog inputs simultaneously at 16-bit resolution at rates of up to 400 kS s^{-1}. During the experiments the DAQ sampled all 7 channels at 1 kHz for each channel, sending the digitized values to the embedded computer for logging. The DAQ also provided the 5 V signal to power the pressure transducers.

Embedded Computer: The DAQ was connected via USB to a mini stick computer with an Intel Atom Z8350 processor, 128GB ROM, and 4GB RAM running the Windows 10 operating system. To minimize RF interference and shield the computer from high altitude radiation, the computer was encased in a copper shield (Figure 3.4a). A custom Matlab script was written to control the acquisition, compiled as a standalone executable. This script allowed for the selection of which channels were to be recorded, the duration of acquisition, and the voltage range at which each channel was recorded. The computer stored all recorded data on its ROM memory which was then downloaded post-flight via the USB connection for archiving and further analysis. To allow payload operational verification, an RS232 connection was established between the computer and the autopilot. Through this channel, sensor voltage variance and preliminary turbulence detection parameters were passed to the autopilot to be included in the telemetry stream.

3.1.3 Flight Profiles:

The flight trajectories for all three flights are presented in Figure 3.5. The flight profiles encompassed balloon launch, ascent to 25 km or 30 km altitude before release of the HiDRON aircraft. Once released, the HiDRON conducted a controlled return to the airspace above the launch and control point, whereby it began a spiraling descent at a nominal descent rate of 2 m s^{-1} (resulting in an overall flight time of

approximately 6 hours). Controlled landing and recovery occurred on the Spaceport America main runway allowing for easy recovery of the aircraft, payload and all logged data.

All three flights started in the early morning hours with Flight 1 launching at 13:47 UTC on June 1 2021, releasing at 14:35 UTC and landing at 18:42. Flight 2 launched at 14:04 UTC on June 4 2021, released at 15:15 UTC and landed at 18:39. Finally, Flight 3 launched at 14:07 UTC on June 6 2021, released at 15:17 UTC and landed at 19:43. Local time at Spaceport America was Mountain Daylight Time (MDT -6:00).

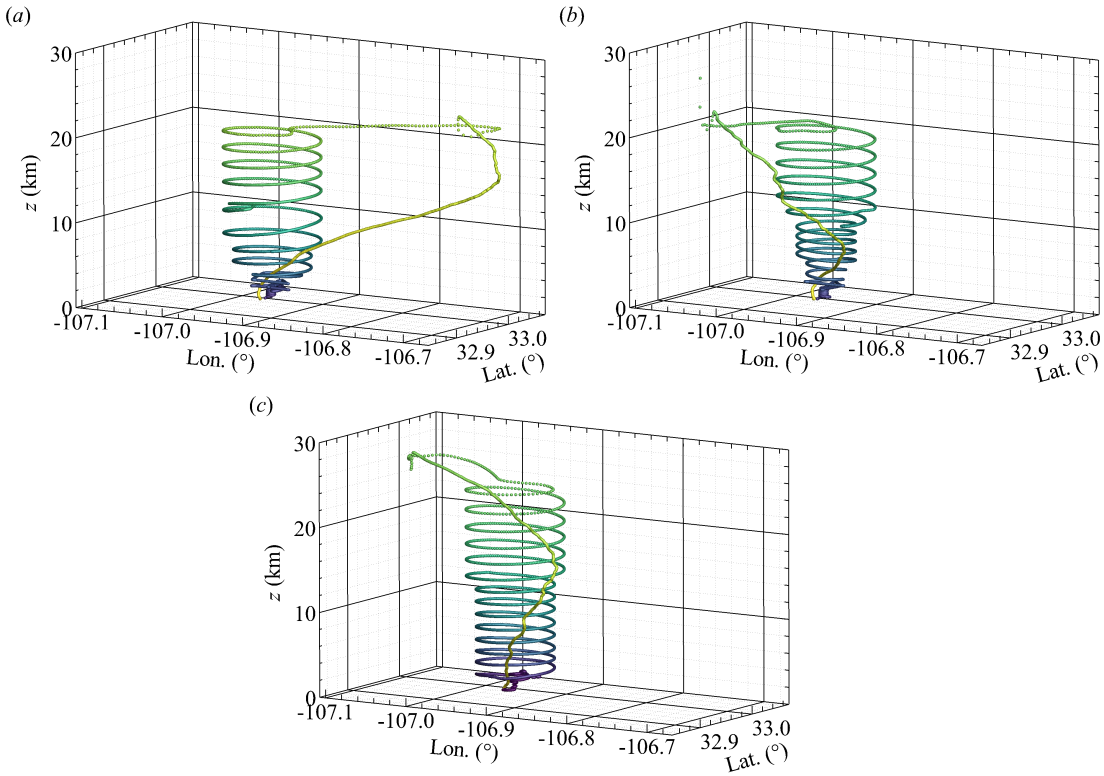

Figure 3.5: HiDRON H2 flight trajectory for (a) Flight 1, (b) Flight 2 and (c) Flight 3. Trajectory is colored by time, with lighter color indicating earliest phase of balloon ascent. z indicates height above ground level (a.g.l.)

Copyright© Anisa Haghighi Najafabadi, 2023.

Chapter 4 In-situ Measurement of Atmospheric Turbulence using the Five-Hole Probe

The material in this chapter presents the results and analysis of the data from the environment sensors and five-hole probe. Results from the infrasonic microphone will be discussed in future work.

The chapter first presents the ambient conditions measured during descent, with the intent of providing the boundary conditions for any turbulent production that may have occurred. Turbulence statistics measured by the five-hole probe during descent are then presented to identify regions where the aircraft flew through turbulence.

As the temperature and humidty sensors were mounted on the upstream side of the wing pillar (as shown in Figure 3.2a), during ascent they were in a stagnant region within the wing pillar wake and therefore not sufficiently aspirated to prevent self-heating and delayed air exchange with the environment. Furthermore, the five-hole-probe was only able to resolve velocity vectors $\pm 30°$ from the probe axis, and was aligned opposite to the direction of flight during the balloon-assisted ascent. Hence, only data from the controlled descent phase of the flight was found to provide reliable results and thus only measurements from the descent are presented in this section. In addition, z is used to indicate altitudes referenced to ground level, i.e. above ground level (a.g.l.) with $z = 0$ referencing the launch and recovery altitude of 1406 m m.s.l.

To obtain statistical properties as a function of z, the time-series during descent was divided into 3 km statistical segments, determined using $|\vec{V}_R|\Delta t$, where Δt is the amount of time included in each segment. Quantities averaged over these segments are indicated using $\langle\ \rangle$ brackets. To increase the spatial resolution of these statistics, each segment is overlapped by 50% (1.5 km). As the separation between each aircraft orbit (Fig. 3.5) was nominally 2 km, these segment sizes were selected to produce statistical bins of approximately equivalent horizontal and vertical separation. Due to the spiralling flight path (as illustrated in Fig. 3.5) each 3.0 km segment represents approximately 200 m of vertical descent, with the overlapping of segments reducing the vertical interval to approximately 100 m.

4.1 Mean Quantities

To establish the ambient conditions during each flight we averaged P, T, RH, U and γ over each statistical segment and compare vertical profiles of these quantities to

publicly-available 12:00 UTC National Weather Service (NWS) radiosonde weather soundings launched from the El Paso (EPZ), Albuquerque (ABQ) and Tuscon (TUS) NWS forecast offices. These forecast offices and sounding times were selected due to their proximity to the launch site and flight times, with the launch site within the triangle formed by these three locations. To assist with comparison across sites in z, we have set $z = 0$ to 1406 m a.g.l. for all profiles. Furthermore, to assist with comparison, the National Oceanic and Atmospheric Administration (NOAA) upper air maps at 250 mb and National Aeronautics and Space Administration (NASA) satellite imagery for the approximate time of Flights 1 through 3 are provided in Appendix 5 with the NWS sounding sites and HiDRON H2 flight location indicated on them. The NWS soundings employed Graw DFM-17 radiosondes with manufacturer-provided accuracies of ± 0.2°C in temperature, $\pm 4\%$ in RH, ± 0.1 m s^{-1} in wind speed and $\pm 1°$ in direction.

Vertical profiles of $\langle T \rangle$ and $\langle RH \rangle$, measured by the HiDRON H2, are compared to the radiosonde profiles for all three flights in Fig. 4.1. The HiDRON H2 temperature is consistent with the trends produced by the radiosonde values, but shows a noticeable warm bias compared to the radiosonde above $z = 16$ km that appears most noticeable for Flight 3. Note that no density correction was applied to this sensor measurement to account for the reduced convective heat transfer at these altitudes.

The profiles of temperature (Fig. 4.1a,b,c) allow identification of the altitudes and properties of the troposphere, tropopause and stratosphere during each flight. The boundary layer height is also roughly identifiable for altitudes lower than 2 km due to the divergence of the profiles caused by the different time of day between the radiosonde and HiDRON H2 measurements. To obtain a more precise estimate of the boundary layer height, the profiles of virtual potential temperature and specific humidity (not shown for the sake of brevity) were examined and the boundary layer heights for each flight were identified by the altitude up to which these quantities were approximately constant. Using the approach, the boundary layer heights were estimated to be at $z = 1.3$ km for Flight 1, $z = 2.1$ km for Flight 2, and $z = 2.2$ km for Flight 3.

For Flight 1, above the boundary layer, a constant lapse rate (the rate of temperature decrease with altitude) of 8.4 °C km^{-1} was measured throughout the troposphere. This lapse rate falls between the values of 9.8 °C km^{-1} usually indicating adiabatic conditions and 6 °C km^{-1} indicating moist adiabatic conditions. This mid range suggests a conditional instability was present during this flight. Specifically, the condition here refers to the potential for clouds to be present [64]. Using the tem-

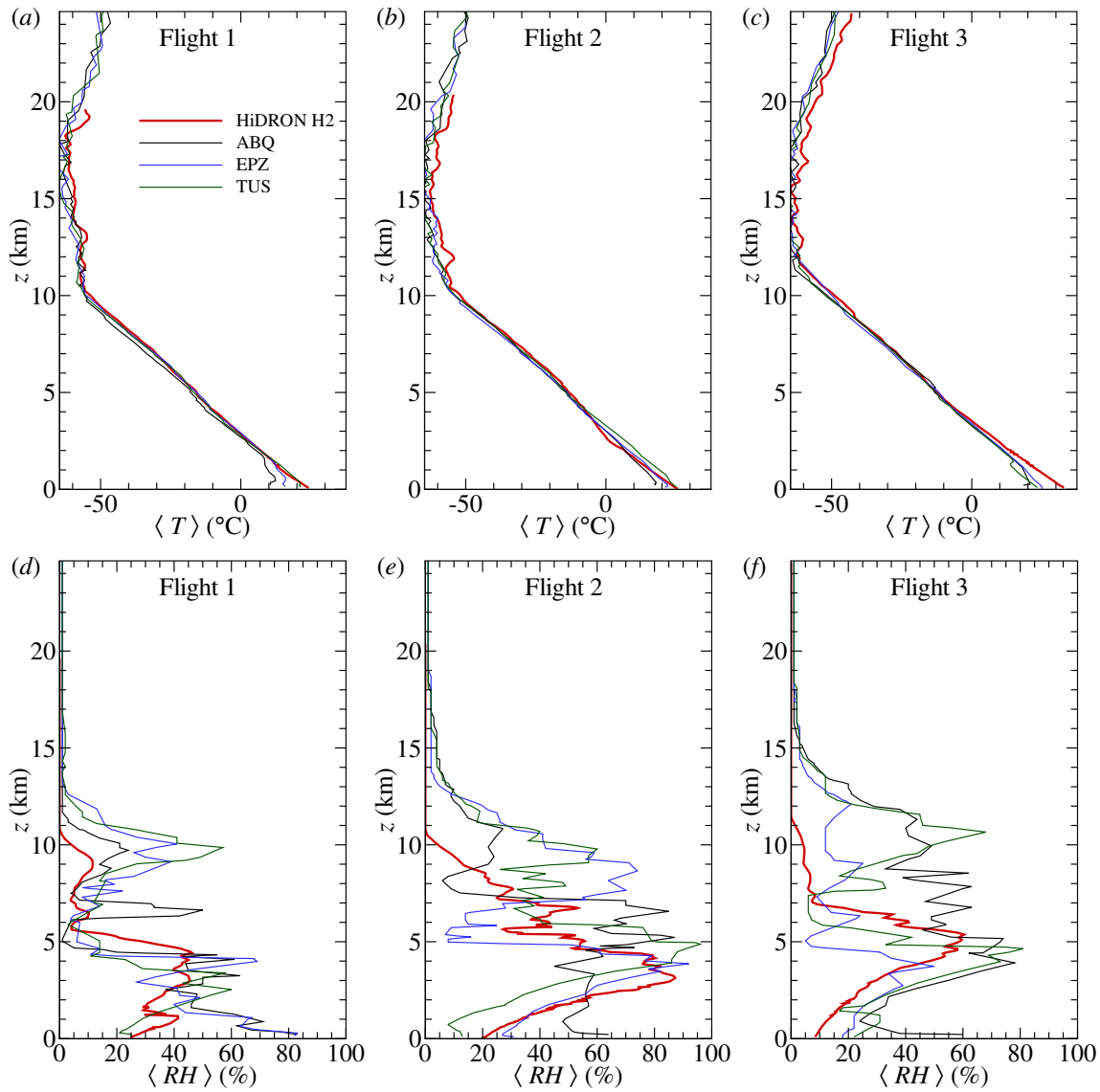

Figure 4.1: Temperature profiles measured during (*a*) Flight 1; (*b*) Flight 2; and (*c*) Flight 3. Corresponding relative humidity profiles shown for (*d*) Flight 1; (*e*) Flight 2; and (*f*) Flight 3.

perature gradient as an indicator, the tropopause occurred at an altitude of 10 km for this flight, above which the temperature continued to decrease with altitude at a rate of 1 °C km^{-1} before the stratospheric temperature inversion (due to heat release via ozone formation) creates a positive temperature gradient with a lapse rate of -5.3 °C km^{-1} above an altitude of 19 km. The temperature inversion results in stable stratification of the air, with little chance of convective instabilities producing turbulence. Furthermore, when stratospheric turbulence is present (e.g. when produced by wind shear), it will tend to be confined to relatively narrow layers in altitude.

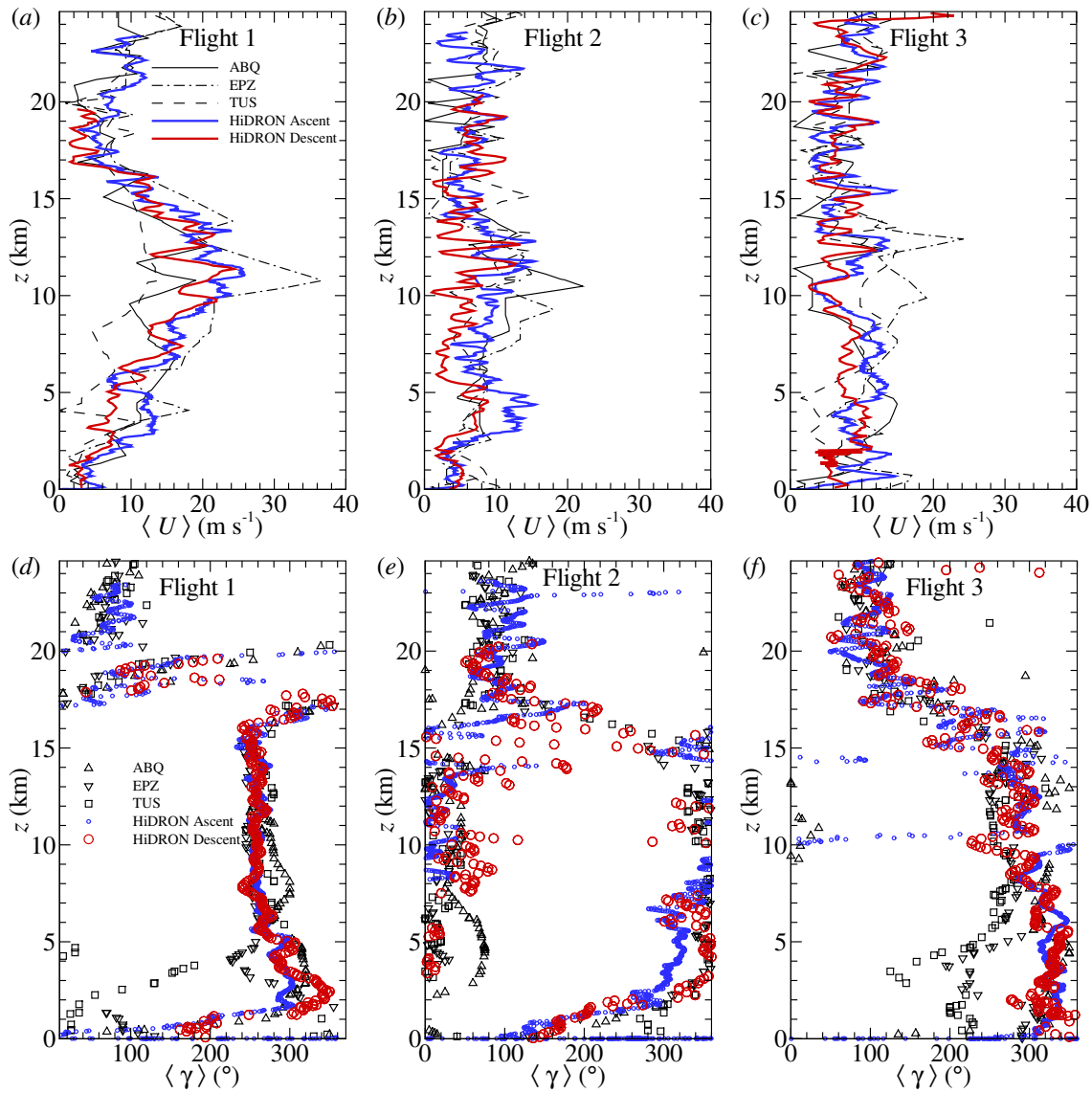

Figure 4.2: Horizontal wind magnitude a measured during (a) Flight 1; (b) Flight 2; and (c) Flight 3. Corresponding wind direction shown for (d) Flight 1; (e) Flight 2; and (f) Flight 3.

Similar temperature conditions were also observed for Flight 2 (Figure 4.1b). The lapse rate measured during this flight was slightly lower at 7.9 °C km^{-1} and the tropopause occurred at a slightly higher altitude of 11.5 km. The temperature gradients in the stratosphere were also reduced, with a lapse rate of 1.6 °C km^{-1} until the temperature inversion at 17 km, above which a gradient of -2.7 °C km^{-1} was measured. Flight 3 (Figure 4.1e) had a tropospheric lapse rate of 8.2 °C km^{-1}, with a slightly higher tropopause measured at 12 km . Finally, a much lower stratospheric temperature inversion was observed on this flight, at only 16 km with a lapse rate of

-3.1 °C km^{-1} above it. There is a short segment of the altitude that the lapse rate falls at 1 °C km^{-1}.

Figures 4.1d-f compare the corresponding $\langle RH \rangle$ measurements from the HiDRON H2 and NWS radiosondes. Significant differences are clearly evident among the profiles. However, noting that the radiosonde data were obtained from disparate locations up to 380 km away from the flight location, differences can be attributed to spatial heterogeneity in the atmospheric moisture concentration. This is qualitatively illustrated by comparison of the cloud coverage in satellite observations (Appendix 5). This was corroborated by cloud height and coverage data retrieved from an Automated Surface Observing System (ASOS) database indicated that the cloud conditions near Truth or Consequences, NM (near Spaceport America) were different from those measured near the other three weather stations mentioned above for the same time period. However, on all three days, the HiDRON H2 reported consistently lower RH values above $z = 7$ km, so a dry bias in the humidity sensor under cold conditions cannot be discounted.

The magnitude and direction of the horizontal winds for all three flights are shown in Fig. 4.2. Again, the wind magnitude and direction measured by the HiDRON H2 compare well with the radiosonde soundings. The strongest winds occurred during Flight 1, with the winds coming from 270° and increasing with altitude to a peak value over 20 m s^{-1} just above the tropopause ($z = 12.5$ km), before decreasing with altitude to the stratospheric inversion near $z = 17$ km. This pattern of constant wind direction and high wind magnitude is consistent with the presence of a jet stream, which was confirmed using upper air wind meteorological maps compiled by NOAA (Appendix 5). These maps indicate that during Flight 1, a tropical jet stream was centered to the southeast of the flight location, over central Texas, such that the flight path was on the outer edge of the jet (Figure A1 a). This jet had dissipated to the east by the time of Flights 2 and 3 (Figures A1 b and A1 c), which is reflected in the reduced magnitude of winds at these altitudes. The relative position of the jet stream for Flight 1 also explains the higher wind magnitudes measured at El Paso, which was closer to the center of the jet. Above the jet stream, the winds increase with altitude again, with significant directionality shifts indicating numerous shear layers were present above the temperature inversion.

Calmer wind conditions were observed during Flights 2 and 3 with magnitudes typically below 10 m s^{-1}, consistently from the north for Flight 2, and some directional shear observed in the radiosonde data above the tropopause between 15 km and 20 km that was not measured by the five-hole probe during Flight 2, but was observed

during Flight 3. Finally, Flight 3, being released from a higher altitude, measured stronger wind magnitudes above 25 km, with peak magnitudes above 20 m s^{-1}.

4.1.1 Stability Conditions

The corresponding Richardson number, Ri, Brunt-Väisälä frequency squared, N^2, and shear frequency S^2 profiles provide some perspective of the resulting atmospheric stability conditions. The square Brunt–Väisälä frequency reflects the static stability and was estimated from

$$N^2 = \frac{g}{\langle\theta_v\rangle}\frac{\partial\langle\theta_v\rangle}{\partial\langle z\rangle}. \tag{4.1}$$

The square shear frequency can also be found from

$$S^2 = \left(\frac{\partial\langle u\rangle}{\partial\langle z\rangle}\right)^2 + \left(\frac{\partial\langle v\rangle}{\partial\langle z\rangle}\right)^2 \tag{4.2}$$

and provides a measure of the possibility of turbulence production by vertical wind shear. The corresponding gradient Richardson number can therefore be found from

$$Ri = \frac{N^2}{S^2}. \tag{4.3}$$

For these calculations, the virtual potential temperature, $\langle\theta_v\rangle$, was calculated by

$$\langle\theta_v\rangle = \langle\theta\rangle\left(1 + (a.r) - r_L - r_I\right) \tag{4.4}$$

where $a = 0.61$ is $g_{air}/g_{watervapor}$,r is water vapor mixing ratio, and r_L is the liquid water mixing ratio, and r_I is ice mixing ratio. For unsaturated air $r_L = 0$. [64].

The helical descent of the aircraft results in approximately 1500 m of horizontal travel for every 100 m of decent and creates some ambiguity in determining the vertical gradients of $\langle\theta_v\rangle$, $\langle u_1\rangle$ and $\langle u_2\rangle$. If we assume horizontal homogeneity of $\langle\theta_v\rangle$, $\langle u_1\rangle$ and $\langle u_2\rangle$ then the vertical gradients can be calculated between neighboring 1500 m statistical segments in time, resulting in a 100 m resolution in the gradient. The profiles of $N = \mathrm{sgn}(N^2)\sqrt{N^2}$ and $S = \mathrm{sgn}(S^2)\sqrt{S^2}$ calculated in this manner (using central differencing between time-adjacent statistical segments) are referred to as N_t and S_t and shown in Fig. 4.3a-c and Fig. 4.3d-f for all three flights respectively.The results show large oscillations with altitude for all three flights. These oscillations are introduced by variability in $\langle u_1\rangle$, $\langle u_2\rangle$ and $\langle\theta_v\rangle$ between each segment (nominally 1500 m) which are amplified by the relatively small difference in $\langle z\rangle$ between each segment (typically around 100 m).

Given that the vertical separation of 100 m also represents a horizontal separation of 1500 m, horizontal velocity and temperature gradients may influence the

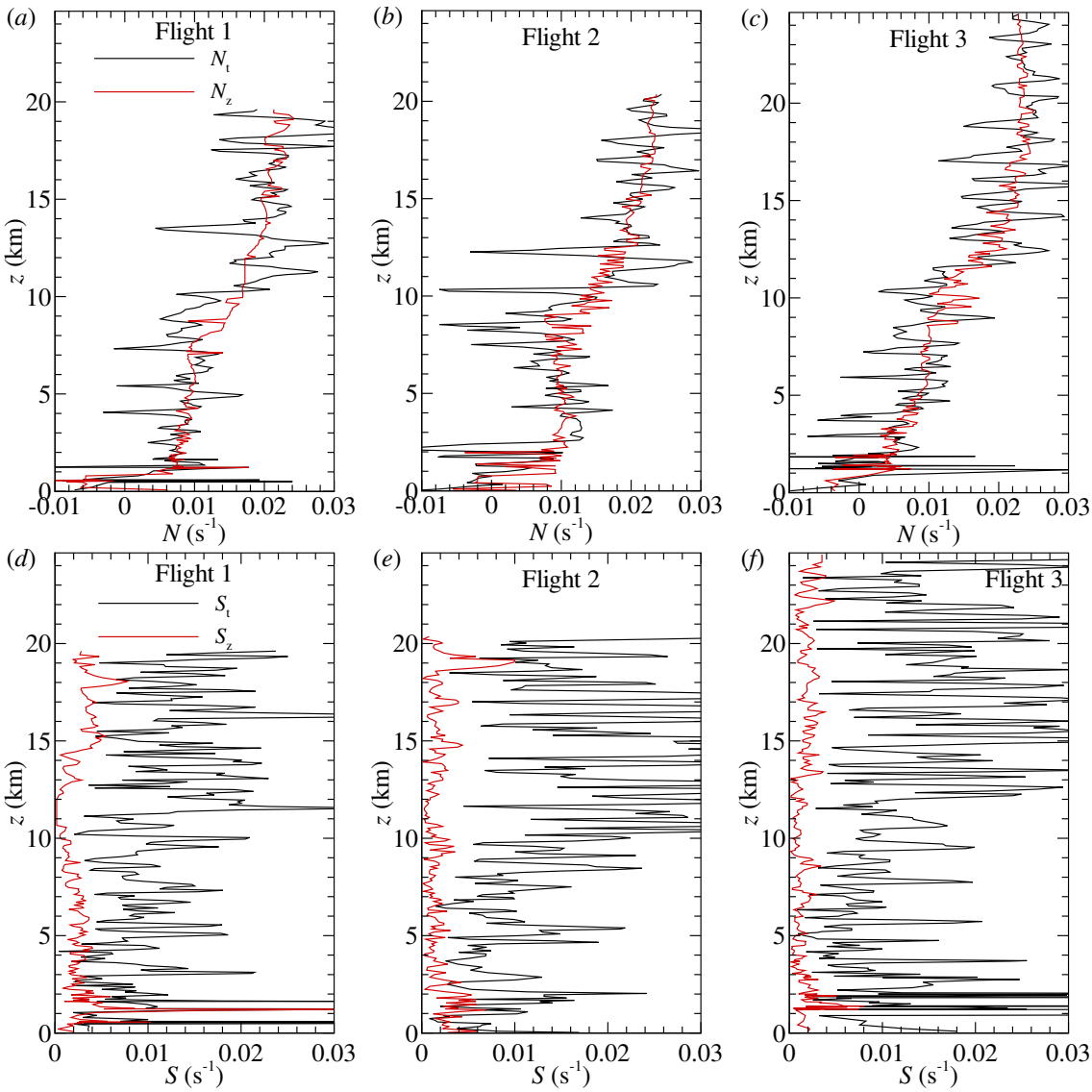

Figure 4.3: Brunt–Väisälä frequency, N_t and N_z, profiles for (a) Flight 1; (b) Flight 2; and (c) Flight 3 and shear frequency, S_t and S_z^2, profiles for (d) Flight 1; (e) Flight 2; and (f) Flight 3.

calculated values of N_t^2 and S_t^2 (Figure 4.3. Hence, an alternative approach was devised to calculate vertical gradient whereby the vertical profiles were expanded along the circumference of the aircraft's orbit, here represented in the form of azimuthal position of the aircraft relative to the center of its orbit, α, which was defined with $\alpha = 0$ directed to the north and increasing positive towards the east. In this manner, $\langle\theta_v\rangle(\alpha, z)$, $\langle u_1\rangle(\alpha, z)$ and $\langle u_2\rangle(\alpha, z)$ were determined. The vertical gradient of each quantity was then found by finding the nearest statistical segments in the positive and negative z directions which minimized the difference in α. These three locations

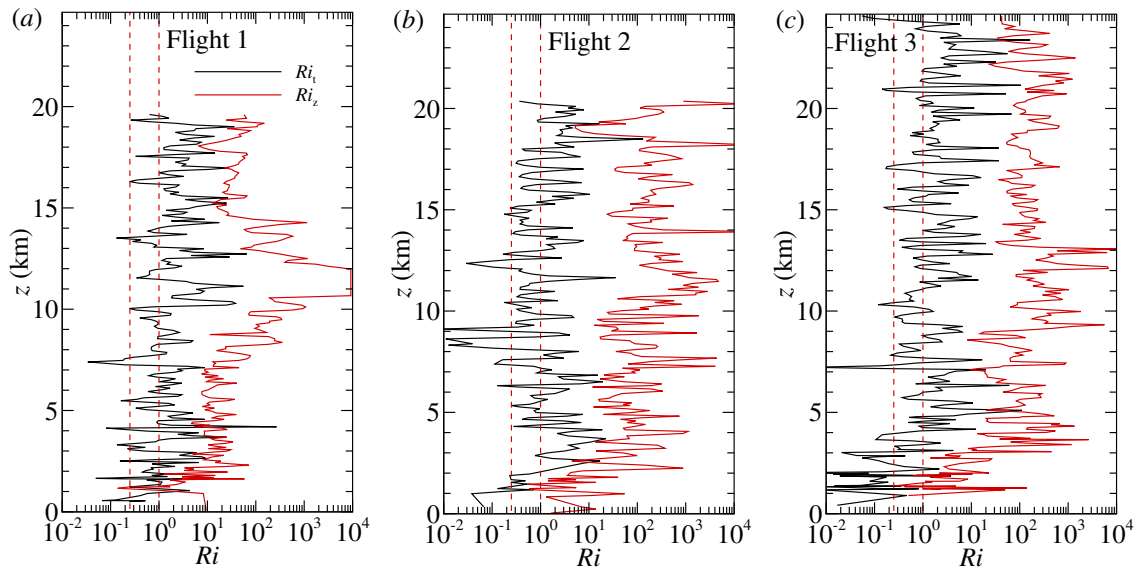

Figure 4.4: Gradient Richardson number, Ri_t and Ri_z, profiles for (a) Flight 1; (b) Flight 2; and (c) Flight 3. The vertical lines indicate $Ri = 0.25$ and $Ri = 1$, denoting the possible range of critical Richardson numbers.

were then used to determine $\partial\langle\theta\rangle/\partial\langle z\rangle$, $\partial\langle u_1\rangle/\partial\langle z\rangle$ and $\partial\langle u_2\rangle/\partial\langle z\rangle$ for the central statistical segment using central differencing, and the resulting N and S profiles are shown on Fig. 4.3, with the results calculated using this approach and referred to as N_z and S_z, respectively. Note that this approach is effectively a gradient calculation across a spatial scale of the same order as the vertical separation between orbits, approximately 2.5 km. However, this gradient calculation could be conducted for every statistical segment, resulting in a temporal resolution of these values that is the same as N_t and S_t. Furthermore, unless the statistical segments were reduced in size, this approach could not resolve the gradients in regions where the horizontal separation between the segments was on the same order as the vertical separation, specifically for the portion of the flight when the aircraft was in a reduced diameter orbit near the landing point ($z < 1$ km) and for a small segment of Flight 1 near $z = 11$ km when the aircraft briefly executed a smaller orbit during its larger orbit (as shown in Fig. 3.5a). For this latter region, the values of N_z and S_z are kept constant in Fig. 4.3.

Fig. 4.3a-c shows that although the N_t and N_z profiles are similar, there are fewer large-scale excursions in N_z. The general trend shows statically near-neutral conditions existed above the boundary layer for Flights 2 and 3, reaching $z = 3$ km for Flight 3. For the remainder of the altitudes measured, the N_z values indicate statically stable conditions existed, with a monotonic increase in N_z with altitude. The

corresponding S_z profiles shown in Fig. 4.3d-f, however,most likely due to the larger vertical distance involved in the differencing, are significantly different in magnitude from their $S_t$counterparts, being typically an order of magnitude lower. The largest difference was observed during Flight 1 near $z = 11$ km, which corresponds to the height where $\langle U \rangle$ is a maximum, resulting in the central differencing across the jet producing mean velocity gradients near zero.

The resulting profiles of Ri are shown in Fig. 4.4a-c for Flights 1 through 3, for both $Ri_t = N_t^2/S_t^2$ and $Ri_z = N_z^2/S_z^2$. For comparison a possible critical Richardson number range of $0.25 < Ri < 1$ [1, 30] is also illustrated on the figures. In general, $Ri_t < 10$ with frequent instances of $Ri_t < 1$. Conversely, $Ri_z > 10$ for the majority of the profile, with low and negative Ri_z measured only in the region near the boundary layer. This roughly two-orders-of-magnitude difference in Ri_t and Ri_z values can be attributed to the order of magnitude difference in S_t and S_z and reflects the sensitivity of Ri to small velocity differences.

4.2 Local Turbulence Measurement

The results presented in the previous section demonstrated that the conditions existed for the production of turbulence during all three flights. Specifically, the Ri and N^2 results indicate conditions conducive to buoyant turbulent production within the boundary layer, and a conditionally unstable troposphere suggests the possibility of localized buoyant production in that atmospheric layer. Furthermore, during Flight 1, significant wind shear was measured in the stratosphere, suggesting the potential for mechanical production in the upper atmosphere.

These properties, however, indicate only that the conditions were present which were conducive to the production of turbulence. The nature of the HiDRON measurements allows the the measurement of different metrics that can be used to confirm the presence of turbulence at different altitudes. One measure of the local turbulence intensity is the turbulent kinetic energy, k. Here, k was calculated as a function of distance along the flight trajectory using

$$k = \frac{1}{2}\left(\langle u_1'^2 \rangle + \langle u_2'^2 \rangle + \langle u_3'^2 \rangle\right) \tag{4.5}$$

where, $u_i'(t) = u_i(t) - \langle u_i \rangle$. Note that since $u_1(t)$, $u_2(t)$ and $u_3(t)$ were oversampled, to minimize the influence of high frequency noise on these quantities, $\langle u_1'^2 \rangle$, $\langle u_2'^2 \rangle$ and $\langle u_3'^2 \rangle$ were calculated by first subtracting $\langle u_1 \rangle$, $\langle u_2 \rangle$ and $\langle u_3 \rangle$ from u_1, u_2 and u_3, respectively, then calculating the velocity spectrum of each velocity component in

the frequency domain for each statistical segment of the time series (here denoted as $F_{uu}(f)$, $F_{vv}(f)$ and $F_{ww}(f)$ respectively, where f is frequency). This was done using Welch's periodogram method implemented with a variance-preserving Hanning window, three subintervals, and a 50% overlap. The low-pass filtered estimates of $\langle u_1'^2 \rangle$, $\langle u_2'^2 \rangle$ and $\langle u_3'^2 \rangle$ were then determined by integrating $F_{uu}(f)$, $F_{vv}(f)$ and $F_{ww}(f)$ over the range $f < 20$ Hz. This threshold was selected to coincide with the maximum frequency at which the probe's response to pressure fluctuations response could be expected to be unity. The resulting profiles of k for all three flights are presented in Fig. 4.5a-c.

For Flight 1 the boundary layer turbulence is clearly evident in Fig. 4.5a as an increase in k for $z < 2$ km, with slightly thicker regions of elevated k evident in Fig. 4.5b and c for $z < 4$ km and $z < 3$ km for Flights 2 and 3. Above these altitudes, the values of k largely remained below unity except in several localized regions where elevated k values were measured. For Flight 1 within the troposphere, these regions occurred at $z \approx 3$ km, 6 km and $z \approx 8$ km, whereas within the stratosphere broadly elevated values of k were observed for $z > 16$ km, with significant increase in k observed at $z = 11.5$ km. Similar behavior was measured during Flights 2 and 3, specifically $k > 1$ near the surface, and isolated and localized regions of enhanced k within the troposphere and stratosphere, although these cases exhibit generally higher k and more variability in the profiles.

The layers of high k at 6 km and 8 km appear to correspond to localized regions of low N and hence Ri (Figures 4.3a and 4.4a), whereas where the layer of high k was observed at 13 km, these metrics indicate stable conditions were present. Instead, looking at the wind profiles in Figure 4.2a as well as the temperature profile in Figure 4.1a, this location is at the interface between the troposphere and tropopause and coincide with a strong wind shear corresponding to the upper half of the jet stream suggesting that this layer of turbulence was produced through mechanical production. A localized temperature inversion was also observed at that altitude which can be attributed to turbulent mixing.

Within the stratosphere during Flight 1, there was an increased level of k measured. This is suggests the presence of stratospheric turbulence on this flight, which can be attributed to production by the wind shear observed (Figure 4.2a). Note that the elevated values of k may not necessarily correspond to velocity fluctuations caused by turbulence. To assess the presence of an inertial subrange corresponding to the existence of a universal equilibrium range within the turbulence, we examine the one-dimensional energy spectra in wavenumber space, here estimated from the

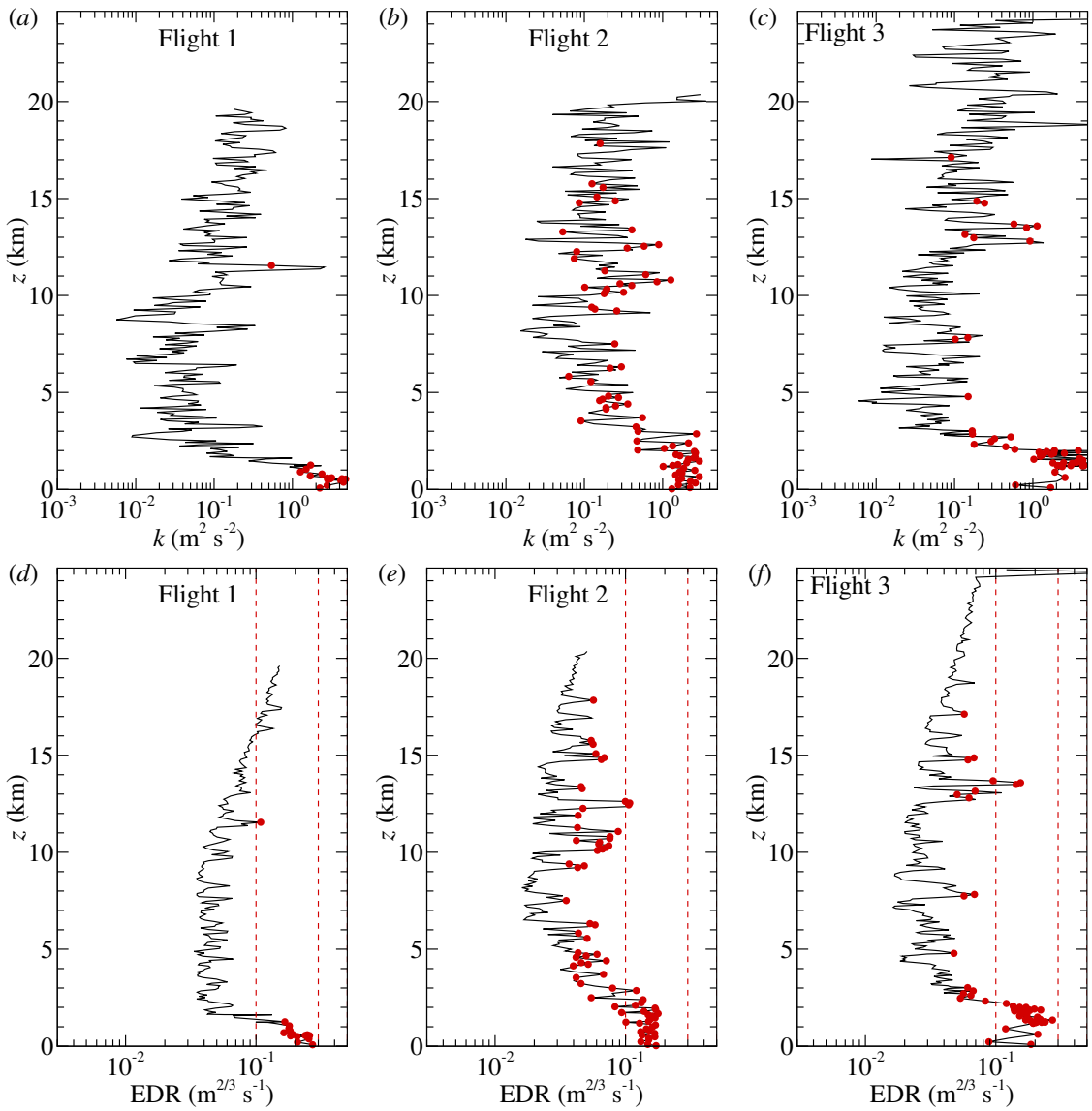

Figure 4.5: Profiles of k for (a) Flight 1, (b) Flight 2, and (c) Flight 3. Corresponding profiles of EDR are shown for (d) Flight 1, (e) Flight 2, and (f) Flight 3. Solid red symbols indicate measurements where $-1.8 < n < -1.5$. Dashed lines indicate qualitative turbulence intensity levels from [36] referred to as: steady for $EDR < 0.1$; weak for EDR between 0.1 and 0.3; moderate for EDR between 0.3 and 0.5; strong for EDR between 0.5 and 0.8; and very strong for $EDR > 0.8$.

longitudinal velocity spectra using the relative velocity of the air relative to the sensor. This velocity spectrum was calculated by first rotating the (u_1, u_2, u_3) coordinate system from the east-north-up alignment to instead align u_1 with an axis parallel to the velocity of the aircraft within the air, i.e. we define $u_\ell(t)$ as the component of the wind velocity vector found by projection of the wind velocity vector, $\vec{U}$, in the direc-

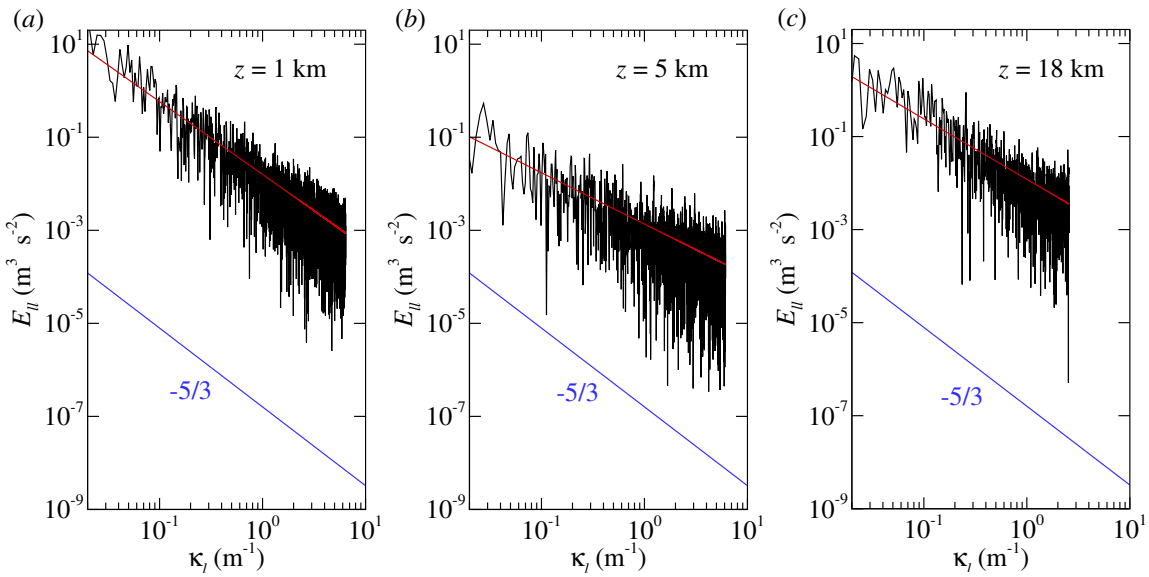

Figure 4.6: Example longitudinal velocity spectra from Flight 1 at (a) $z = 1$ km, (b) $z = 10$ km, and (c) $z = 18$ km. Red lines indicate fit, blue lines indicate $f^{-5/3}$ slope. Only content for wavenumbers corresponding to $f < 20$ Hz are shown.

tion formed by $\langle \vec{V}_G - \vec{U} \rangle$. The velocity spectrum of $u_\ell(t)$ in the frequency domain, $F_{\ell\ell}(f)$, was calculated on the rotated wind velocity vector.

To transform the velocity spectrum in the frequency domain to the wavenumber domain, the longitudinal wavenumber, κ_ℓ, was then approximated using Taylor's frozen-flow hypothesis such that $\kappa_\ell \approx f 2\pi |\langle \vec{V}_R \rangle|^{-1}$. We then found the longitudinal velocity spectrum in the wavenumber domain as $E_{\ell\ell} = F_{\ell\ell} |\langle \vec{V}_R \rangle| (2\pi)^{-1}$, where this last operation was conducted to ensure that integrating $E_{\ell\ell}(\kappa_\ell)$ in κ_ℓ produced the variance of u_ℓ.

Example longitudinal velocity spectra in the wavenumber domain are shown in Fig. 4.6 which demonstrate, as evident in Fig. 4.6b,c,that although the spectra indicate a broadband energy content within the five-hole-probe sensor's response range ($f < 20$ Hz), the spectra can display some deviation from the characteristic $-5/3$ slope associated with the locally isotropic turbulence expected within the inertial subrange [42].

We then identify instances where a turbulent inertial subrange is present as instances where the power law fit of Bf^n to $E_{\ell\ell}(\kappa_\ell)$ (in the range $\kappa_\ell > 0.1$ m^{-1}, $f < 20$ Hz) produced exponent values within the range of $-1.8 < n < -1.5$, corresponding to $-5/3 \pm 10\%$. When these instances are isolated (as indicated by solid red symbols in Fig. 4.5a-c), very few turbulent regions become evident for Flight 1. However, for Flights 2 and 3 (Fig. 4.5b and c) this criteria becomes less discriminat-

ing, which may correspond to the increased fluctuations in the profiles of k during these flights. For all three flights a layer of high k was observed in a region near the tropopause. It was found that for regions where turbulence was not detected, n trended towards -1, which is believed to be the roll-off of the background sensor noise.

For Flights 2 and 3, turbulent kinetic energy profiles are more scattered, potentially due to increased uncertainty in the u_1, u_2 measurement due to the tubing disconnection noted during these flights (as discussed in Section 3.1.2). This uncertainty could cause increases in measured k as a result of inaccurately resolving the change of direction of the aircraft, particularly during sudden movements. However, it is also possible that the increased scatter is simply due to the reduced winds during these flights, resulting an a lower signal-to-noise ratio in the measured frequency content.

Distinguishable spikes in k are still observed, however. For Flight 2, the Ri profiles (Figure 4.4b) indicate unstable conditions below approximately 3 km, associated with the convective boundary layer. Figure 4.5b shows that these conditions produced turbulence convecting up to and through the boundary layer and capping inversion at altitudes of 5 km. Several layers of instability as reflected by $Ri < 0.25$ in Figure 4.4b were also observed in the troposphere for this flight, and corresponding elevated layers of k can be observed in Figure 4.5b, indicating several regions of localized buoyantly-driven turbulence. Unstable conditions in the tropopause at an altitude of 13 km were also observed which also corresponds to significantly increased $\langle k \rangle / \langle U \rangle^2$ at this altitude. The Ri observations for Flight 2 indicate that stable conditions existed above 15 km. However the wind direction within the tropopause changed significantly between 15 km and 20 km during this flight (Figure 4.2b) and thus the potential to be turbulence produced by the mean wind shear. However, although there is elevated k in the stratosphere for this flight, this turbulence could not be attributed to either buoyant or shear production, and may be advected into the measurement domain.

Flight 3 had a more stable troposphere (Figure 4.4c), which is also reflected in the reduced levels of k between 5 km and 15 km relative to Flight 2. However, there were regions of negative Ri at 10 km and 12 km that correspond to regions of elevated $\langle k \rangle / \langle U \rangle^2$. Interestingly, the high The high k observed from 13 km to 15 km does not appear to correspond to either buoyant or shear production, as Ri at this altitude does suggests stable conditions and no significant wind shear was observed at that altitude, although wind shear was observed above 18 km which appears to correspond to additional peaks in k. As with Flight 2, although there is elevated

k in the stratosphere, it could not be directly attributed to either buoyant or shear production.

Noting that for equilibrium, homogeneous, turbulence, production and dissipation tend to be in balance and therefore an alternative measure of the turbulence magnitude that is often used is the turbulent kinetic energy dissipation rate, ε. As described in Section 2.3, the corresponding statistic of eddy dissipation rate, EDR, is often used in the aviation industry to identify regions of high turbulence. One advantage of using ε as a metric for the presence of atmospheric turbulence is that ε is a small-scale phenomenon and one does not need to resolve the largest scales of turbulence in order to obtain a measure of the turbulence. Hence, whereas the window size used to determine k will tend to bias its value towards the intensity of scales resolved by the window, EDR will be more effective at identifying more intense regions of turbulence.

However, as the five-hole-probe measurements lacked the spatio-temporal resolution required to determine ε directly through Equation 2.10, an indirect estimate of ε was needed to determine $EDR = \varepsilon^{1/3}$. To do so, we assume the presence of sufficiently high Reynolds number for the formation of an inertial subrange in the energy spectrum. Under such conditions, the one-dimensional longitudinal wavenumber velocity spectrum in the inertial subrange is expected to follow a scaling such that

$$E_{\ell\ell}(\kappa_\ell) = 0.49\varepsilon^{2/3}\kappa_\ell^{-5/3} \tag{4.6}$$

following Equation 2.15 [e.g. 54]. For the present measurements, this scaling was used to estimate ε by fitting a power-law, i.e. $A\kappa_\ell^n$, to $E_{\ell\ell}$ over the κ_ℓ range corresponding to $\kappa_\ell > 0.1$ and $f < 20$ Hz, thus allowing the estimate

$$\varepsilon = \left(\frac{A}{0.49}\left(\kappa_\ell\right)^{5/3}\right)^{3/2} \tag{4.7}$$

to be made for each statistical segment. The low wavenumber bound of $\kappa_\ell = 0.1$ was determined by inspection of the longitudinal velocity spectra and identifying the range of vales which exhibited power law decay.

Note that this approach will provide a non-zero value for ε even if no turbulence is present, and therefore some caution is required when interpreting EDR beyond being a qualitative indication of the presence of turbulence in the form of localized regions of relatively high EDR. However, one advantage of using the spectral roll-off for determining ε is that it will discriminate between velocity fluctuations caused by turbulence, (i.e. with a $-5/3$ roll-off) and that caused by other sources of velocity

Turbulence Intensity	Steady	Weak	Moderate	Strong	Very Strong
***EDR* Range**	<0.1	0.1-0.3	0.3-0.5	0.5-0.8	>0.8

Table 4.1: EDR ranges identified to correspond to different turbulence intensities.

fluctuation (e.g. via aircraft maneuvering) which will have very different spectral content.

Figure 4.5d-f shows the resulting profiles of EDR measured for Flights 1, 2 and 3, respectively. When compared to k, there are fewer regions of turbulence identified using this metric, as it tends to bias towards the more intense regions of turbulence. Using the EDR ranges provided by Table 4.1, indicated by the dashed lines on Figure 4.5d-f, certain altitudes in each flight can be identified and classified as possible encounters of turbulence.

For example, the EDR indicates that the aircraft experienced turbulence during Flight 1 (Figure 4.5d) at several locations: within the boundary layer ($z < 2$ km); in the stratosphere ($z > 18$ km); and in the troposphere in weak thin layers . Turbulence was identified at the interface between the troposphere and tropopause at $z = 12$ km. In the mid-tropospheric altitudes weak to moderate turbulence was measured at several altitude levels. Interestingly, although comparison of the EDR results (Figure 4.5d) and k results (Figure 4.5a) show both statistics generally identify the same locations of turbulence, the relative intensities are noticeably different in some instances reflecting the scale dependence of these statistical measures of turbulence. Combining the results for Ri, N_t^2 and S_t^2 and EDR, several regions of potential flight through turbulence were identified for Flight 1 and related to their production mechanisms and summarized in Table 4.2.

As with Flight 1, in Flight 2, the EDR profiles appear to generally identify the same locations as k for the presence of turbulence, however the relative severity of the turbulence is frequently different. For example, Figure 4.5e shows several peaks of enhanced EDR measured for Flight 2 around $z = 15$ km, whereas these peaks blend in with the background k fluctuations. Furthermore, numerous weak and moderate regions of turbulence were identified as local peaks in EDR for all flights. The Flight 3 EDR profiles (Figure 4.5f) suggest slightly calmer conditions existed during this flight than during Flight 2. Although there were fewer layers where peaks in EDR were measured, the peaks that were present were stronger. A summary of the turbulent regions detected during Flights 2 and 3, along with their production mechanisms inferred from the N_t and S_t profiles, are provided in Tables 4.4 and 4.3.

z **(km)**	EDR	**Production Mechanism**
0-1.5	0.1-0.3	buoyant boundary layer
2.5	0.05	unknown, advection?
3.5	0.05	shear
4.5	0.05	buoyant
5.5	0.05	buoyant
7-8	0.05	buoyant
12	0.1	shear
13-14	0.08	buoyant
15.5-16.5	0.1	shear
17.5	0.1	unknown, advection?
19-20	0.1-0.2	shear

Table 4.2: Turbulence location, intensity and production mechanism summary for Flight 1.

z **(km)**	EDR	**Production Mechanism**
0-2	0.2	buoyant boundary layer
4-5.5	0.06	unknown, advection?
6	0.05	shear
7.5	0.04	buoyant
8-9	0.01	buoyant
10-11.5	0.08	shear and buoyant
12-13	0.1	shear and buoyant
13.5-15.5	0.05-0.08	shear
16-18	0.06 intermittent	shear

Table 4.3: Turbulence location, intensity and production mechanism summary for Flight 2.

z **(km)**	EDR	**Production Mechanism**
0-2	0.5	buoyant and shear boundary layer
3-4	0.05	buoyant&shear
7	0.02	buoyant
9-11	0.03	unknown, advection?
13-14	0.1	shear
15	0.07	shear
16-17	0.07	shear
21	0.05	shear
25	0.4	shear

Table 4.4: Turbulence location, intensity and production mechanism summary for Flight 3.

Chapter 5 Conclusions and Future Work

This work demonstrates how a UAS in the form of a balloon-launched glider can be used to conduct detailed analysis of the statistical structure of the atmosphere over a range of altitudes typically interrogated using weather balloons. In the measurements described here, the particular aircraft was equipped with a five-hole-probe for measuring the three-component wind vector, and a pressure, temperature and humidity sensing system integrated into the aircraft.

These instruments allowed the calculation of vertical profiles of T, RH, U and γ which compared favorably with publicly-available radiosonde data from the National Weather Service. In addition, the slow, spiralling descent allowed for the calculation of spatially-averaged statistics such as k and ε with high vertical resolution. The resulting vertical profiles suggest that isolated regions of turbulence were present in all three flights, although enhanced values of ε in the stratosphere, represented using EDR, were produced despite the kinetic energy content not containing the characteristic roll-off expected for inertial range turbulence. However, there is some ambiguity in Richardson number calculation introduced by the spiral flight path into the vertical gradient calculation. One approach taken to resolve this ambiguity, was to determine the vertical gradients normal to the spiraling path (rather than using the gradients along the flight path) provided promising results, but resulted in significant reduction in the vertical resolution of the calculation.

Despite this ambiguity, these initial flights suggest that the UAS measurements have the potential to make connections between regions of increased turbulence and their generating mechanisms. From a purely statistical viewpoint, the ability of the aircraft to orbit around a fixed geographical point, rather than travelling with the wind, eases horizontal localization of the measurements. In addition, the flight pattern allows for increased statistical convergence due to the larger volume of air sampled over a particular altitude range. To highlight this point, for a 1000 m of altitude change, during the experiments described here, the orbit of the UAS allowed it to sample the atmosphere for a distance of approximately 15,000 m, whereas comparable in-situ measurements by a balloon would have sampled only the 1000 m column along its ascent path.

This data set therefore offers a rich opportunity to explore the dynamics of turbulence in the atmosphere. Future work will focus on more detailed statistical analysis,

including examining the altitude dependence of the Reynolds stress distributions and corresponding anisotropy, examining the suitability of different length scales used for describing atmospheric turbulence, and revisiting the use of the Richardson number as a metric to describe the potential for turbulence to exist. The helical trajectory taken by the glider during its descent also introduces the possibility of producing depictions of the horizontal heterogeneity of multiple parameters measured during the descent making it possible to visualize the structure of the atmospheric motions measured along the flight path.

A secondary objective of this study was to assess the feasibility of implementing an infrasonic microphone on a UAS for detecting clear air turbulence. Although preliminary analysis of the microphone response has been conducted, suggesting that the infrasonic microphone can detect turbulent features, particularly near the stronger boundary layer turbulence. However, for the weaker tropospheric and stratospheric turbulence experienced during these flights, it was difficult to conclusively link regions of higher infrasonic noise detection to higher turbulence once out of the boundary layer. These difficulties were contributed to by the remote-sensing nature of this instrument, its altitude sensitivity, and the broad-band nature of turbulent sound generation, which make it challenging to discriminate discrete turbulent events. Future work will analyze these signals in much more detail, to try to resolve some of these ambiguities. Finally, one of the more significant challenges involved with this work is that the non-stationarity of the atmosphere makes it difficult to draw firm conclusions from just three flights. Therefore, this series of flights can, and should, be succeeded with many more. In addition to providing a broader range of conditions to analyze, additional flights can be used to improve the measurement systems themselves. In particular, it would be highly beneficial to increase instrumentation sensitivity (e.g. through amplification of the five-hole-probe and microphone signal), reduce background noise (e.g. by shielding temperature and humidity probes from solar radiation, adding acoustic materials and analog filters to the microphone), and introduce new sensing capabilities (e.g. hot-wire probes with high frequency response and sensitivity, particulate counters and spectrometers for ice particulate detection, gas sensors for greenhouse case sensing).

Copyright© Anisa Haghighi Najafabadi, 2023.

Appendix: Upper Air Maps

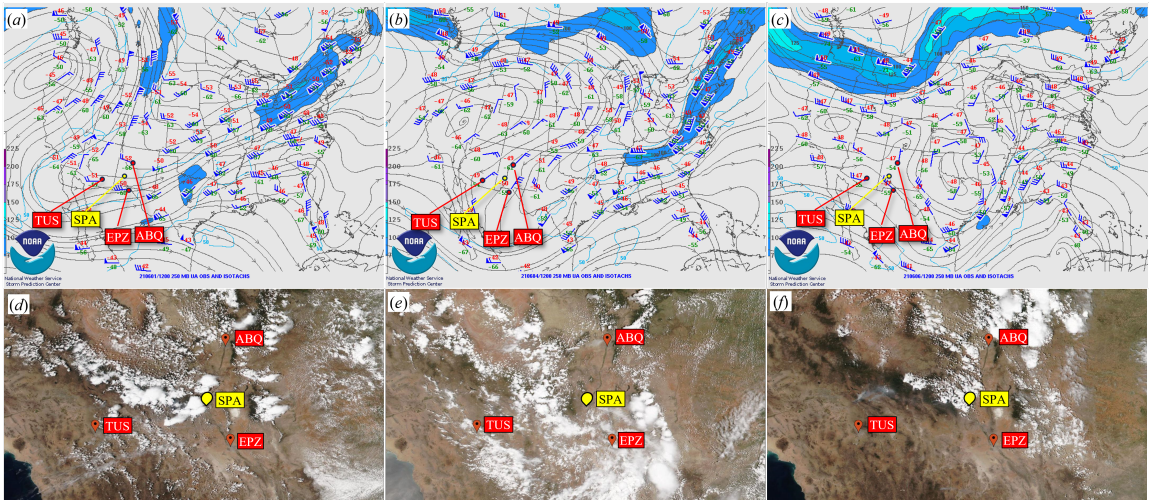

Figure A1: NOAA Jet stream maps at 250 mb (10.366 km) for (a) Flight 1, (b) Flight 2, (c) Flight 3 and satellite images of cloud cover for (d) Flight 1, (e) Flight 2, (f) Flight 3. Red pins indicate NWS sounding sites and yellow pin indicates measurement location. (NASA)

Bibliography

[1] H. D. I. Abarbanel, D. D. Holm, J. E. Marsden, and T. Ratiu. Richardson number criterion for the nonlinear stability of three-dimensional stratified flow. *Phys. Rev. Lett.*, 52:2352–2355, Jun 1984.

[2] L. Al-Ghussain and S. C. C. Bailey. An approach to minimize aircraft motion bias in multi-hole probe wind measurements made by small unmanned aerial systems. *Atmospheric Measurement Techniques*, 14(1):173–184, 2021.

[3] L. Al-Ghussain and S. C. C. Bailey. Uncrewed aircraft system measurements of atmospheric surface-layer structure during morning transition. *Boundary-Layer Meteorology*, 185(2):229–258, Nov 2022.

[4] J.-R. Alisse, P. H. Haynes, J. Vanneste, and C. Sidi. Quantification of stratospheric mixing from turbulence microstructure measurements. *Geophysical Research Letters*, 27(17):2621–2624, 2000.

[5] D. Anfossi, G. Schayes, G. Degrazia, and A. Goulart. Atmospheric turbulence decay during the solar total eclipse of 11 august 1999. *Boundary-Layer Meteorology*, 111(2):301–311, May 2004.

[6] S. Bailey, G. Kunkel, M. Hultmark, M. Vallikivi, J. Hill, K. Meyer, C. Tsay, C. Arnold, and A. Smits. Turbulence measurements using a nanoscale thermal anemometry probe. *Journal of Fluid Mechanics*, 663:160–179, Nov. 2010.

[7] S. C. C. Bailey, C. A. Canter, M. P. Sama, A. L. Houston, and S. W. Smith. Unmanned aerial vehicles reveal the impact of a total solar eclipse on the atmospheric surface layer. *Proceedings of the Royal Society A: Mathematical, Physical and Engineering Sciences*, 475(2229):20190212, 2019.

[8] S. C. C. Bailey, G. J. Kunkel, M. Hultmark, M. Vallikivi, J. P. Hill, K. A. Meyer, C. Tsay, C. B. Arnold, and A. J. Smits. Turbulence measurements using a nanoscale thermal anemometry probe. *J. Fluid Mech.*, 663:160–179, 2010.

[9] B. B. Balsley, D. A. Lawrence, R. F. Woodman, and D. C. Fritts. Fine-scale characteristics of temperature, wind, and turbulence in the lower atmosphere (0–1,300 m) over the south peruvian coast. *Boundary-Layer Meteorology*, 147(1):165–178, 2013.

[10] L. Barbieri, S. T. Kral, S. C. C. Bailey, A. E. Frazier, J. D. Jacob, J. Reuder, D. Brus, P. B. Chilson, C. Crick, C. Detweiler, A. Doddi, J. Elston, H. Foroutan, J. González-Rocha, B. R. Greene, M. I. Guzman, A. L. Houston, A. Islam, O. Kemppinen, D. Lawrence, E. A. Pillar-Little, S. D. Ross, M. P. Sama, D. G. Schmale, T. J. Schuyler, A. Shankar, S. W. Smith, S. Waugh, C. Dixon, S. Borenstein, and G. de Boer. Intercomparison of small unmanned aircraft system (sUAS) measurements for atmospheric science during the LAPSE-RATE campaign. *Sensors*, 19(9), 2019.

[11] K. Bärfuss, F. Pätzold, B. Altstädter, E. Kathe, S. Nowak, L. Bretschneider, U. Bestmann, and A. Lampert. New setup of the UAS ALADINA for measuring boundary layer properties, atmospheric particles and solar radiation. *Atmosphere*, 9(1), 2018.

[12] D. Bohn and H. Simon. Mehrparametrige approximation der eichräume und eichflächen von unterschall-bzw. überschall-5-loch-sonden. *tm-Technisches Messen*, 468(JG):81–89, 1975.

[13] T. A. Bonin, A. Choukulkar, W. A. Brewer, S. P. Sandberg, A. M. Weickmann, Y. L. Pichugina, R. M. Banta, S. P. Oncley, and D. E. Wolfe. Evaluation of turbulence measurement techniques from a single Doppler lidar. *Atmospheric Measurement Techniques*, 10(8):3021–3039, 2017.

[14] D. C. Bowman and J. M. Lees. Infrasound in the middle stratosphere measured with a free-flying acoustic array. *Geophysical Research Letters*, 42(22), nov 2015.

[15] R. Calmer, G. C. Roberts, J. Preissler, K. J. Sanchez, S. Derrien, and C. O'Dowd. Vertical wind velocity measurements using a five-hole probe with remotely piloted aircraft to study aerosol–cloud interactions. *Atmospheric Measurement Techniques*, 11(5):2583–2599, 2018.

[16] C. Canter and S. Bailey. Spatially sampled turbulence measurements acquired using unmanned aerial vehicles. In *Bulletin of the American Physical Society Division of Fluid Dynamics*, Atlanta, GA, November 2018. American Physical Society.

[17] J. I. Cardesa, A. Vela-Martín, and J. Jiménez. The turbulent cascade in five dimensions. *Science*, 357(6353):782–784, 2017.

[18] A. chaman motlagh, V. Ahmadi, and K. Abedi. The effect of atmospheric turbulence on the performance of the free space optical communications. pages 540 – 543, 08 2008.

[19] C. E. Christenson, J. E. Martin, and Z. J. Handlos. A synoptic climatology of northern hemisphere, cold season polar and subtropical jet superposition events. *Journal of Climate*, 30(18):7231 – 7246, 2017.

[20] I. P. Chunchuzov, S. N. Kulichkov, O. E. Popov, and V. G. Perepelkin. Infrasound generation by meteorological fronts and its propagation in the atmosphere. 2021.

[21] L. H. Clem. Clear-air turbulence near the jet-stream maxima. *Bulletin of the American Meteorological Society*, 36(2):53–60, 1955.

[22] P. Cunningham and D. Keyser. Synoptic meteorology — jet streaks. In G. R. North, J. Pyle, and F. Zhang, editors, *Encyclopedia of Atmospheric Sciences*, pages 359–369. Academic Press, Oxford, second edition, 2015.

[23] J. Cuxart, D. Tatrai, T. Weidinger, A. Kircsi, J. Józsa, and M. Kiss. Infrasound as a detector of local and remote turbulence. *Boundary-Layer Meteorology*, 159(2):185–192, oct 2015.

[24] A. Desai, W. E. Heilman, N. S. Skowronski, K. L. Clark, M. R. Gallagher, C. B. Clements, and T. Banerjee. Features of turbulence during wildland fires in forested and grassland environments. *Agricultural and Forest Meteorology*, 338:109501, July 2023.

[25] J. A. Dutton and H. A. Panofsky. Clear air turbulence: A mystery may be unfolding. *Science*, 167(3920):937–944, 1970.

[26] L. J. Ehrenberger. Stratospheric turbulence measurements and models for aerospace plane design. Technical Report TM-104262, NASA, Dec. 1992.

[27] R. Enlich and R. Mancuso. The turbulence climatology of the United States between 20,000 and 45,000 feet estimated from aircraft reports and meteorological data. Technical report, Stanford Research Institute, June 1968.

[28] J. Faber, M. Gerding, A. Schneider, A. Dörnbrack, H. Wilms, J. Wagner, and F.-J. Lübken. Evaluation of wake influence on high-resolution balloon-sonde measurements. *Atmospheric Measurement Techniques*, 12(8):4191–4210, 2019.

[29] T. Foken. *Micrometeorology*. Springer, 2008.

[30] B. Galperin, S. Sukoriansky, and P. S. Anderson. On the critical Richardson number in stably stratified turbulence. *Atmospheric Science Letters*, 8(3):65–69, 2007.

[31] N. M. Gavrilov, H. Luce, M. Crochet, F. Dalaudier, and S. Fukao. Turbulence parameter estimations from high-resolution balloon temperature measurements of the MUTSI-2000 campaign. *Annales Geophysicae*, 23(7):2401–2413, 2005.

[32] F. Girard-Ardhuin, B. Bénech, B. Campistron, J. Dessens, and S. Jacoby-Koaly. Remote sensing and surface observations of the response of the atmospheric boundary layer to a solar eclipse. *Boundary-Layer Meteorology*, 106(1):93–115, Jan 2003.

[33] J. Gonzalo, D. López, D. Domínguez, A. García, and A. Escapa. On the capabilities and limitations of high altitude pseudo-satellites. *Progress in Aerospace Sciences*, 98:37–56, 2018.

[34] A. Haack, M. Gerding, and F.-J. Lübken. Characteristics of stratospheric turbulent layers measured by LITOS and their relation to the Richardson number. *Journal of Geophysical Research: Atmospheres*, 119(18):10,605–10,618, sep 2014.

[35] S. Hobbs, D. Dyer, D. Courault, A. Olioso, J.-P. Lagouarde, Y. Kerr, J. McAnneney, and J. Bonnefond. Surface layer profiles of air temperature and humidity measured from unmanned aircraft. *Agronomie*, 22(6):635–640, 2002.

[36] R. Huang, H. Sun, C. Wu, C. Wang, and B. Lu. Estimating eddy dissipation rate with QAR flight big data. *Applied Sciences*, 9(23):5192, nov 2019.

[37] P. Høeg, R. Prasad, and K. Borre. Impact of atmosphere turbulence on satellite navigation signals. pages 231–239, 2008.

[38] J. D. Jacob, P. B. Chilson, A. L. Houston, and S. W. Smith. Considerations for atmospheric measurements with small unmanned aircraft systems. *Atmosphere*, 9(7), 2018.

[39] P. Jayakrishnan, C. Babu, and S. P. Drastic variation in the surface boundary layer parameters over cochin during the annular solar eclipse: Analysis using sonic anemometer data. *Journal of Atmospheric and Solar-Terrestrial Physics*, 94:49 – 53, 2013.

[40] L. Kantha, D. Lawrence, H. Luce, H. Hashiguchi, T. Tsuda, R. Wilson, T. Mixa, and M. Yabuki. Shigaraki UAV-radar experiment (ShUREX): overview of the campaign with some preliminary results. *Progress in Earth and Planetary Science*, 4(1), jul 2017.

[41] S.-H. Kim, H.-Y. Chun, J.-H. Kim, R. D. Sharman, and M. Strahan. Retrieval of eddy dissipation rate from derived equivalent vertical gust included in aircraft meteorological data relay (AMDAR). *Atmospheric Measurement Techniques*, 13(3):1373–1385, 2020.

[42] A. N. Kolmogorov. The local structure of turbulence in incompressible viscous fluid for very large reynolds numbers. *Dokl. Akad. Nauk SSSR*, 30:301–305, 1941.

[43] C. L. Korb, B. M. Gentry, and C. Y. Weng. Edge technique: theory and application to the lidar measurement of atmospheric wind. *Appl. Opt.*, 31(21):4202–4213, Jul 1992.

[44] D. A. Lawrence and B. B. Balsley. High-resolution atmospheric sensing of multiple atmospheric variables using the DataHawk small airborne measurement system. *Journal of Atmospheric and Oceanic Technology*, 30(10):2352–2366, 2013.

[45] D. Lenschow. *The measurement of air velocity and temperature using the NCAR Buffalo aircraft measuring system.* National Center for Atmospheric Research, 1972.

[46] M. Mauder, M. Eggert, C. Gutsmuths, S. Oertel, P. Wilhelm, I. Voelksch, L. Wanner, J. Tambke, and I. Bogoev. Comparison of turbulence measurements by a CSAT3B sonic anemometer and a high-resolution bistatic Doppler lidar. *Atmospheric Measurement Techniques*, 13(2):969–983, 2020.

[47] F. J. Merceret. Measuring atmospheric turbulence with airborne hot-film anemometers. *Journal of Applied Meteorology (1962-1982)*, 15(5):482–490, 1976.

[48] P. Moin and K. Mahesh. Direct numerical simulation: A tool in turbulence research. *Annual Review of Fluid Mechanics*, 30(1):539–578, 1998.

[49] R. T. Palomaki, N. T. Rose, M. van den Bossche, T. J. Sherman, and S. F. D. Wekker. Wind estimation in the lower atmosphere using multi-rotor aircraft. *Journal of Atmospheric and Oceanic Technology*, Early online release, 2017.

[50] F. Payne and J. Lumley. One-dimensional spectra derived from an airborne hot-wire anemometer. *Quarterly Journal of the Royal Meteorological Society*, 92:397–401, 1966.

[51] S. B. Pope. *Turbulent Flows*. Cambridge University Press, 2000.

[52] E. S. Posmentier. 1- to 16-hz infrasound associated with clear air turbulence predictors. *Journal of Geophysical Research*, 79(12):1755–1760, apr 1974.

[53] A. Rautenberg, M. S. Graf, N. Wildmann, A. Platis, and J. Bange. Reviewing wind measurement approaches for fixed-wing unmanned aircraft. *Atmosphere*, 9(11):1–24, 2018.

[54] S. G. Saddoughi and S. V. Veeravalli. Local isotropy in turbulent boundary layers at high Reynolds number. *J. Fluid Mech.*, 268:333–372, 1994.

[55] T. J. Schuyler, S. C. C. Bailey, and M. I. Guzman. Monitoring tropospheric gases with small unmanned aerial systems (sUAS) during the second CLOUDMAP flight campaign. *Atmosphere*, 10(8), 2019.

[56] P. Sekula, M. Zimnoch, J. Bartyzel, A. Bokwa, M. Kud, and J. Necki. Ultra-light airborne measurement system for investigation of urban boundary layer dynamics. *Sensors*, 21(9), 2021.

[57] Q. A. Shams, A. J. Zuckerwar, C. G. Burkett, G. R. Weistroffer, and D. R. Hugo. Experimental investigation into infrasonic emissions from atmospheric turbulence. *The Journal of the Acoustical Society of America*, 133(3):1269–1280, mar 2013.

[58] R. D. Sharman, L. B. Cornman, G. Meymaris, J. Pearson, and T. Farrar. Description and derived climatologies of automated in situ eddy-dissipation-rate reports of atmospheric turbulence. *Journal of Applied Meteorology and Climatology*, 53(6):1416–1432, jun 2014.

[59] R. D. Sharman, S. B. Trier, T. P. Lane, and J. D. Doyle. Sources and dynamics of turbulence in the upper troposphere and lower stratosphere: A review. *Geophysical Research Letters*, 39(12), 2012.

[60] H. Siebert, K. Lehmann, and R. A. Shaw. On the use of hot-wire anemometers for turbulence measurements in clouds. *Journal of Atmospheric and Oceanic Technology*, 24(6):980 – 993, 2007.

[61] J. Söder, M. Gerding, A. Schneider, A. Dörnbrack, H. Wilms, J. Wagner, and F.-J. Lübken. Evaluation of wake influence on high-resolution balloon-sonde measurements. *Atmospheric Measurement Techniques*, 12(8):4191–4210, 2019.

[62] L. N. Storer, P. D. Williams, and P. G. Gill. Aviation turbulence: Dynamics, forecasting, and response to climate change. *Pure and Applied Geophysics*, 176(5):2081–2095, 2019.

[63] R. Stull. *An Introduction to Boundary Layer Meteorology*. Springer, 1988.

[64] R. Stull. *Meteorology for Scientists and Engineers*. BC Open Textbook Collection. Department of Earth, Ocean & Atmospheric Sciences, 2011.

[65] J. Söder, C. Zülicke, M. Gerding, and F.-J. Lübken. High-resolution observations of turbulence distributions across tropopause folds. *Journal of Geophysical Research: Atmospheres*, 126(6), mar 2021.

[66] H. Tennekes and J. L. Lumley. *A First Course in Turbulence*. The MIT Press, Cambridge, Massachusetts, 1972.

[67] B. Thies and J. Bendix. Satellite based remote sensing of weather and climate: recent achievements and future perspectives. *Meteorological Applications*, 18(3):262–295, 2011.

[68] A. L. Treaster and A. M. Yocum. The calibration and application of five-hole probes. Technical report, DTIC Document, 1978.

[69] A. Tsinober. *An Informal Introduction to Turbulence*, volume 63. Springer Science & Business Media, 2001.

[70] A. van den Kroonenberg, T. Martin, M. Buschmann, J. Bange, and P. Vörsmann. Measuring the wind vector using the autonomous mini aerial vehicle M^2AV. *J. Atmos. Oceanic Technol.*, 25:1969–1982, 2008.

[71] A. van den Kroonenberg, T. Spieß, M. Buschmann, T. Martin, P. Anderson, F. Beyrich, and J. Bange. Boundary layer measurements with the autonomous mini-UAV M^2AV. In *Proceedings of DACH2007*, Hamburg, Germany, 2007.

[72] S. Vogt and P. Thomas. Sodar — a useful remote sounder to measure wind and turbulence. *Journal of Wind Engineering and Industrial Aerodynamics*, 54-55:163–172, 1995. Third Asian-Pacific Symposium on Wind Engineering.

[73] S. Vogt and P. Thomas. Sodar — a useful remote sounder to measure wind and turbulence. *Journal of Wind Engineering and Industrial Aerodynamics*, 54-55:163–172, 1995. Third Asian-Pacific Symposium on Wind Engineering.

[74] J. Wescott. *Acoustic Detection of High - Altitude Turbulence*. Defense Technical Information Center, 1964.

[75] N. Wildmann, M. Hofsäß, F. Weimer, A. Joos, and J. Bange. Masc–a small remotely piloted aircraft (RPA) for wind energy research. *Advances in Science and Research*, 11(1):55–61, 2014.

[76] J. Williams and G. Meymaris. *Remote Turbulence Detection Using Ground-Based Doppler Weather Radar*, pages 149–177. 06 2016.

[77] B. M. Witte, R. F. Singler, and S. C. Bailey. Development of an unmanned aerial vehicle for the measurement of turbulence in the atmospheric boundary layer. *Atmosphere*, 8(10):195, 2017.

[78] R. Worthington. Tropopausal turbulence caused by the breaking of mountain waves. *Journal of Atmospheric and Solar-Terrestrial Physics*, 60(16):1543–1547, 1998.

[79] J. C. Wyngaard. *Turbulence in the Atmosphere*. Cambridge University Press, 2010.

Vita

Anisa Haghighi Najafabadi

Education:

- University of Kentucky, Lexington, KY
  M.S. in Mechanical Engineering, In Progress
- York University, Toronto, ON
  B.Sc. in Physics and Astronomy, June 2013

Professional Positions:

- Research Assistant, University of Kentucky January 2020-Present

Publications & Preprints:

- Haghighi, A. N., Nolin, R. D., Pundsack, G. D., Craine, N., Stratislatau, A., and Bailey, S. C. C.: High-altitude atmospheric turbulence and infrasound measurements using a balloon-launched small uncrewed aircraft system, EGUsphere [preprint], https://doi.org/10.5194/egusphere-2023-633, 2023.